THE STEADY-STATE STRUCTURE OF RELATIVISTIC MAGNETIC JETS

Mark R. Dubal
Center for Relativity
The University of Texas at Austin
Austin, Texas 78712-1081
USA

Ornella Pantano
Dipartimento di Fisica 'G. Galilei'
via Marzolo 8
35131 Padova, Italy

June 1992

The steady-state structure of relativistic magnetic jets

Mark R Dubal[1] and Ornella Pantano[2]

[1]Center for Relativity, University of Texas at Austin, Austin, Texas 78712-1081, USA

[2]Dipartimento di Fisica 'G. Galilei', via Marzolo 8, 35131 Padova, Italy

Abstract. The method of characteristics is used to study the structure of steady, relativistic jets containing a toroidal magnetic field component. We assume axisymmetry and perfect conductivity for the fluid flows. Oblique, relativistic, magnetic shocks are handled using a shock fitting procedure. The effects of the magnetic field on the collimation and propagation of the jets are studied when the external medium has a constant or decreasing pressure distribution. Our parameter study is confined to underexpanded jet flows which have an ultra-relativistic equation of state and extremely supermagnetosonic bulk velocities. The magnetic energy density, however, may range from zero to extreme dominance. These simulations are therefore relevant to compact radio jet sources which exhibit superluminal motion.

For slightly underexpanded jets propagating into a constant pressure external medium the jet structure is quite periodic. This periodicity is enhanced as the toroidal field strength increases and the jet is strongly pinched. Recollimation occurs whether or not a toroidal field is present.

When the jet propagates into an external medium of decreasing pressure its structure is very dependent upon the pressure gradient. For a pressure law $p \propto z^{-2}$, where z is the distance from the jet source, the periodic structure is lost. A non-magnetic jet expands freely into the external medium and eventually comes into pressure equilibrium with it. A toroidal magnetic field cannot stop the jet from expanding. When $p \propto z^{-1}$ a semi-periodic structure is regained; again this periodicity is particularly noticeable when a strong toroidal field is present. Also in this case, however, the magnetic field cannot prevent the jet from expanding, although it can reduce greatly the rate at which it does so.

1. Introduction

Many observations of extragalatic radio sources show highly collimated jets of gas emanating from a central galaxy. These outflows, possibly composed of electron-proton or electron-positron relativistic plasma, sometimes exhibit apparent superluminal motions, implying relativistic bulk velocities with Lorentz factors of $\Gamma \sim 10$ (Zensus and Pearson 1987). The radiation from the jets is typically highly polarized and follows a power-law spectrum, indicating emission by the synchrotron process. This characteristic signature in turn denotes the presence of magnetic fields, which, in many cases, will play a significant role in determining the jet structure. It is well known, for example, that helical fields are capable of collimating plasma streams via the pinch effect. In the case of high power radio jets, measurements of the X-ray emissivity indicate that the pressure of the surrounding medium alone is insufficient to confine the jet material, and therefore magnetic fields must be invoked. Moreover, with suitable magnetic field configurations, it is possible to reduce the tendency of jet disruption by Kelvin-Helmholtz and other shearing instabilities (Ferrari *et al* 1981). This would then allow the formation of jets with lengths $\sim 10^3$ times their beam radius.

Thus it is clear that both relativistic motion and magnetic fields play dominant roles in determining the structure of astrophysical jets. For this reason in this paper we construct jet models by solving numerically the equations of special relativistic magnetohydrodynamics (MHD). Our models necessarily have a number of simplifying assumptions; in particular we assume axisymmetric, adiabatic and steady flows with only a toroidal magnetic field component. These assumptions require some justification since real jets are three-dimensional, lose energy by radiative mechanisms and are turbulent to some extent.

The two-dimensional nature of our calculations is in the spirit of previous numerical jet investigations (see for example Norman and Winkler 1984, Kössl *et al* 1990a,b,c), i.e. that much can be learned from such simulations before moving onto more complex and costly three-dimensional models. Since our jet flows are stationary we do not model instabilities, axisymmetric or otherwise, and therefore we are neglecting completely the turbulent sheath that appears in the dynamical simulations of Norman and Winkler and others. Sanders (1983), Wilson and Falle (1985) and Falle and

Wilson (1985) have investigated some of the properties of steady hydrodynamical jets in the context of active galaxies. Close to the jet source (or nozzel) steady flow is thought to be a good approximation and therefore structures similar to those seen in laboratory jets may appear. Significant portions of the jet could be steady in very high Mach number flows where large scale features respond slowly to pressure changes (Falle 1991). Thus our interest is in the average overall structure of the jet, i.e. the shape of the boundary and the positions of prominent features such as knots and wiggles etc. which vary slowly when compared to longitudinal flow time-scales. Perturbation theory also indicates that highly relativistic flows are stabilized against shearing instabilities, and that the presence of a magnetic field enhances this stability still further (Ferrari *et al* 1981). Such results need to be verified in the non-linear regime by the use of high resolution time-dependent relativistic MHD codes (Dubal 1991), however for the present we take the perturbation results to indicate that a turbulent sheath (if one should form) plays a minor role in the overall jet structure. It would be interesting to test whether the steady jet models we construct are indeed stable.

Our approach to solving the relativistic MHD equations employs the method of characteristics, which requires that the system of partial differential equations be purely hyperbolic. This means that in steady two-dimensional flow the (magnetoacoustic) Mach number must always be greater than one and no dissipative terms can be handled. The neglect of radiation losses in the jet flow is probably the most serious approximation we make. Wilson (1987b) has modelled relativistic steady jets which are supersonic along their entire length. Many shocks occur so that the gas remains very hot and an ultra-relativistic equation of state (adiabatic index $\gamma = 4/3$) is appropriate.

The method of characteristics is well suited to studying the structure of steady jets (Courant and Friedrichs 1948, Anderson 1982; for astrophysical applications see Sanders 1983 and Daly and Marscher 1988). Its power lies in the fact that domains of influence and dependence are modelled precisely, and thus it is possible to treat waves and discontinuities with high accuracy and efficiency. A number of three-dimensional characteristic techniques do exist, however they are complicated and, unlike the two-dimensional case, the approach is not unique, leading to hybrid schemes which often lose the original power of the characteristic approach. Therefore we have chosen to

start with the simpler two-dimensional problem.

In principle our approach can handle any (axisymmetric) magnetic field configuration, however we include only a toroidal component, h^θ, since this is the most important one for collimation of the jet material (Kössl *et al* 1990c). It is probable that h^θ helps confine the jet at the nozzel exit (Wardle and Potash 1982); a large h^θ can stabilize the nozzel wall, reducing incursion of wall material into the jet and preventing its fragmentation by Kelvin-Helmholtz instabilities. In addition hose-pipe motions are reduced if the toroidal field is present in a surrounding conducting sheath, while beam disruption due to pinching modes is reduced if velocities are highly relativistic. Therefore the transverse field, $h_\perp$, would be large near the nozzel and would decay as the jet expands, while the parallel field, $h_\parallel$, increases due to the shearing of $h_\perp$ and dominates far from the source region. A large $h_\parallel$ at the source can disrupt nozzel formation, thus any asymmetry in the magnetic field configuration can lead to one-sided jets (Benford 1987).

Taking into account the above discussion we aim to model high Mach number compact jets close enough to the nozzel region that h^θ dominates, but sufficiently far that the flow is already supermagnetosonic and therefore the gravitational influence of the primary energy source (a black hole or otherwise) may be neglected.

The plan of this paper is as follows. In the next section we derive the characteristic and compatibility equations for two-dimensional (axisymmetric), relativistic gas flows with a single toroidal magnetic field component. Following analogous work in aerodynamic nozzel design we rewrite the equations in terms of quantities which simplify the task of numerically solving these equations via the method of characteristics. Internal shocks can occur in the jet and their trajectories must be tracked across the characteristic grid. Therefore in section 3 we discuss the relations between the values of the fluid variables on either side of a relativistic, magnetic, oblique shock surface. In section 4 the numerical approach is described in detail. Section 5 presents first some tests of the numerical code and then a parameter survey of the general flow properties of the jets. In particular we study the effect of an increasingly large toroidal magnetic field on the initial expansion of the jet in constant and decreasing pressure external mediums. Some conclusions are drawn in section 6.

2. The characteristic form of the Relativistic MHD equations

The equations which describe the flow of a perfectly conducting, non-self-gravitating relativistic fluid in the presence of a magnetic field are, (i) the conservation of baryons, (ii) the conservation of energy-momentum and (iii) Maxwell's equations. These may be written down as (e.g. Lichnerowicz 1967; Anile 1989),

$$\nabla_\alpha(\rho u^\alpha) = 0, \qquad \nabla_\alpha T^{\alpha\beta} = 0, \qquad \nabla_\alpha(u^\alpha h^\beta - u^\beta h^\alpha) = 0 \tag{1}$$

where ρ is the rest-mass density, u^α is the 4-velocity of the fluid, $T^{\alpha\beta}$ is the total stress-energy tensor and h^α represents the magnetic field. The symbol ∇_α denotes the covariant derivative compatible with a ***flat*** spacetime metric $g^{\alpha\beta}$. For a perfect (non-viscous) fluid the total stress-energy tensor takes the following form;

$$T^{\alpha\beta} = (e + p + \mu|h|^2)u^\alpha u^\beta + (p + \frac{1}{2}\mu|h|^2)g^{\alpha\beta} - \mu h^\alpha h^\beta \tag{1b}$$

where p is the isotropic fluid pressure, e is the total fluid energy density, μ is the magnetic permeability and $|h|^2 = h_\alpha h^\alpha > 0$. Note that the magnetic field is defined such that $u^\alpha h_\alpha = 0$, i.e. h^α is orthogonal to the fluid 4-velocity. The quantities ρ, p and e are all measured in the fluid comoving frame. We are assuming isotropy and infinite conductivity of the fluid, so that the conductivity $\sigma^{\alpha\beta} = \sigma_0 g^{\alpha\beta}$ with $\sigma_0 \to \infty$ and thus the field is frozen into the fluid. The speed of light is taken to be unity.

To complete the system of equations (1) we need to add an appropriate equation of state of the form

$$p = p(e, S) \tag{2}$$

where S is the specific entropy. From Anile and Pennisi (1985) the system (1) may be manipulated to give,

$$e'_p u^\alpha \nabla_\alpha p + (e + p)\nabla_\alpha u^\alpha = 0 \tag{3a}$$

$$u^\alpha \nabla_\alpha S = 0 \tag{3b}$$

$$u^\alpha \nabla_\alpha h^\beta - h^\alpha \nabla_\alpha u^\beta + (u^\beta h^\alpha - e'_p h^\beta u^\alpha)\frac{\nabla_\alpha p}{(e + p)} = 0 \tag{3c}$$

$$(e+p+\mu|h|^2)u^\alpha\nabla_\alpha u^\beta - \mu h^\alpha\nabla_\alpha h^\beta + (g^{\alpha\beta}+2u^\alpha u^\beta)\mu h_\nu\nabla_\alpha h^\nu + \frac{1}{(e+p)}[(e+p)g^{\alpha\beta}+(e+p-e'_p\mu|h|^2)u^\alpha u^\beta + \mu h^\alpha h^\beta]\nabla_\alpha p = 0 \quad (3d)$$

$$u^\alpha u^\beta\nabla_\alpha h_\beta + \nabla_\alpha h^\alpha = 0, \quad (3e)$$

where

$$e'_p = (\partial e/\partial p)_S = 1/v_S^2 \qquad \text{and therefore} \qquad e'_p - 1 = (1-v_S^2)/v_S^2 = 1/c_S^2. \quad (4)$$

Here v_S is the thermal sound speed of the fluid and $c_S = \Gamma_S v_S$, where $\Gamma(v) = (1-v^2)^{-1/2}$ is the usual special relativistic Lorentz factor.

In this paper we will use a cylindrical coordinate system (t, r, θ, z), but consider only steady, $(\partial/\partial t = 0)$, axi-symmetric jets (i.e. no θ dependence) with a single toroidal magnetic field component h^θ. Thus we can write $u^\alpha = \Gamma(1, v^r, 0, v^z)$ and $h^\alpha = (0, 0, h^\theta, 0)$ since $u^\alpha h_\alpha = 0$. In this case there is never a time component of h^α. Then the system of equations (3) produces, firstly from (3a),

$$c'_p\left(v^r\frac{\partial p}{\partial r}+v^z\frac{\partial p}{\partial z}\right)+(e+p)\left\{\frac{\partial v^r}{\partial r}+\frac{\partial v^z}{\partial z}+\frac{v^r}{r} + \Gamma^2\left[(v^r)^2\frac{\partial v^r}{\partial r}+v^rv^z\left(\frac{\partial v^r}{\partial z}+\frac{\partial v^z}{\partial r}\right)+(v^z)^2\frac{\partial v^z}{\partial z}\right]\right\} = 0 \quad (5a)$$

and secondly from (3b),

$$v^r\frac{\partial S}{\partial r}+v^z\frac{\partial S}{\partial z} = 0. \quad (5b)$$

The t, r and z components of equation (3c) are identically zero, while the θ component gives,

$$v^r\frac{\partial h^\theta}{\partial r}+v^z\frac{\partial h^\theta}{\partial z}-\frac{e'_p h^\theta}{(e+p)}\left(v^r\frac{\partial p}{\partial r}+v^z\frac{\partial p}{\partial z}\right) = 0. \quad (5c)$$

The r and z components of equation (3d) can be manipulated, using the t component, to produce

$$w\Gamma^2\left(v^r\frac{\partial v^r}{\partial r}+v^z\frac{\partial v^r}{\partial z}\right)+\mu h_\theta\frac{\partial h^\theta}{\partial r}+\frac{\partial p}{\partial r} = 0 \quad (5d)$$

and

$$w\Gamma^2\left(v^r\frac{\partial v^z}{\partial r}+v^z\frac{\partial v^z}{\partial z}\right)+\mu h_\theta\frac{\partial h^\theta}{\partial z}+\frac{\partial p}{\partial z} = 0 \quad (5e)$$

respectively. Note that equation (3e) is satisfied trivially. In equations (5d) and (5e) we have written $w = e + p + \mu(h^\theta)^2$ which is the relativistic enthalpy of the fluid plus the magnetic contribution. Equation (5b) indicates that the fluid motion is adiabatic, however this condition is satisfied trivially by our choice of a perfect fluid equation of state and therefore (5b) can be discarded. This does introduce a small error at strong shock fronts (Sanders 1983), but for weak or moderate shocks it is quite accurate. The remaining equations of the system (5) need to be solved for the unknown quantities p, h^θ, v^r and v^z. In order to achieve this they will be written as compatibility equations holding along characteristic curves.

We first look for combinations of (5) such that the new system has the form,

$$\frac{\partial \boldsymbol{U}}{\partial z}+\mathbf{A}\cdot\frac{\partial \boldsymbol{U}}{\partial r}+\boldsymbol{B} = 0 \quad (6)$$

where the state vector $\boldsymbol{U}^{\mathrm{T}} = (p, h^\theta, v^r, v^z)$. We find that

$$\mathbf{A} = \begin{pmatrix} (1+1/B)\,v^r/v^z & (\mu h^\theta/B)v^r/v^z & w\Gamma^2v^z/B & -w\Gamma^2v^r/B \\ Cv^r/v^z & [1+(A-1)/B]v^r/v^z & Cw\Gamma^2v^z & -Cw\Gamma^2v^r \\ 1/(w\Gamma^2v^z) & \mu h^\theta/(w\Gamma^2v^z) & v^r/v^z & 0 \\ -v^r/(wBc_S^2) & -\mu h^\theta v^r/(wBc_S^2) & -A/B & \Gamma^2v^rv^z/(Bc_S^2) \end{pmatrix} \quad (7)$$

and

$$\boldsymbol{B}^{\mathrm{T}} = \left(\frac{\omega}{Br}\Gamma^2v^rv^z,\ \frac{C\omega}{r}\Gamma^2v^rv^z,\ 0,\ -\frac{A}{Br}v^r\right) \quad (8)$$

where

$$A = \Gamma_S^2\frac{c_A^2}{c_S^2}+1, \qquad B = \frac{(\Gamma v^z)^2}{c_S^2}-A \qquad \text{and} \qquad C = \frac{(A-1)}{B\mu h^\theta}. \quad (9)$$

In the expression for A we have defined the quantity $c_A = \Gamma_A v_A$ where,

$$v_A = \left[\mu(h^\theta)^2/w\right]^{1/2} \quad (10)$$

which is the relativistic Alfvén wave velocity in the rest frame of the fluid (see Appl and Camenzind 1988; Sloan and Smarr 1987).

The eigenvalues of the matrix $\mathbf{A}$ are found to be, the double root,

$$\lambda_0 = \frac{v^r}{v^z} \quad (11)$$

representing the Alfvén and slow magnetoacoustic waves, and

$$\lambda_{\pm} = \frac{M^r M^z \pm \sqrt{AM^2 - A^2}}{(M^z)^2 - A} \tag{12}$$

representing the fast magnetoacoustic waves. Here M^i is the relativistic Mach number defined by $M^i = \Gamma v^i / c_S$, and $M^2 = M^i M_i$. The system (6) is now re-written as,

$$\boldsymbol{l}_i \cdot \frac{\partial \boldsymbol{U}}{\partial z} + \lambda_i \boldsymbol{l}_i \cdot \frac{\partial \boldsymbol{U}}{\partial r} + \boldsymbol{l}_i \cdot \boldsymbol{B} = 0 \qquad \text{with} \qquad i = 0, \pm \tag{13}$$

where $\boldsymbol{l}_i$ denotes the left eigenvectors which are found by solving $\boldsymbol{l}_i \cdot \mathbf{A} = \lambda_i \boldsymbol{l}_i$. From (7) the left eigenvectors are found to be, first, using (12),

$$\boldsymbol{l}_{\pm} = \left(1, \mu h^{\theta}, \pm \frac{Aw\Gamma^2 v^z}{\sqrt{AM^2 - A^2}}, \mp \frac{Aw\Gamma^2 v^r}{\sqrt{AM^2 - A^2}}\right). \tag{14}$$

Then from (11), since λ_0 is a double root there are two eigenvectors associated with this solution, we find

$$\boldsymbol{l}_0^I = \left(0, \frac{A\mu h^{\theta}}{(A-1)\Gamma^2 v^z w}, \frac{v^r}{v^z}, 1\right) \qquad \text{and} \qquad \boldsymbol{l}_0^{II} = \left(\frac{A}{\Gamma^2 v^z w}, 0, \frac{v^r}{v^z}, 1\right). \tag{15}$$

The compatibility equations are then,

$$\boldsymbol{l}_i \cdot \mathrm{d}\boldsymbol{U} + \boldsymbol{l}_i \cdot \boldsymbol{B} \mathrm{d}z = 0 \qquad \text{along} \qquad \frac{\mathrm{d}r}{\mathrm{d}z} = \lambda_i. \tag{16}$$

From (16) for the case of $\lambda_i = \lambda_{\pm}$ we have that

$$\mathrm{d}p + \mu h^{\theta} \mathrm{d}h^{\theta} \pm \frac{Aw\Gamma^2 v^z}{\sqrt{AM^2 - A^2}} \mathrm{d}v^r \mp \frac{Aw\Gamma^2 v^r}{\sqrt{AM^2 - A^2}} \mathrm{d}v^z + \frac{Aw\Gamma^2}{B} \left[v^z \pm \frac{Av^r}{\sqrt{AM^2 - A^2}}\right] \frac{v^r}{r} \mathrm{d}z = 0 \tag{17}$$

which are satisfied along the characteristic curve

$$\frac{\mathrm{d}r}{\mathrm{d}z} = \frac{M_r M_z \pm \sqrt{AM^2 - A^2}}{B}, \tag{18}$$

while for $\lambda_i = \lambda_0$, we obtain

$$I \qquad \frac{A\mu h^{\theta}}{(A-1)\Gamma^2 v^z w} \mathrm{d}h^{\theta} + \frac{v^r}{v^z} \mathrm{d}v^r + \mathrm{d}v^z = 0 \tag{19}$$

and

$$II \qquad \frac{A}{\Gamma^2 v^z w} \mathrm{d}p + \frac{v^r}{v^z} \mathrm{d}v^r + \mathrm{d}v^z = 0 \tag{20}$$

which both hold along the characteristic curve

$$\frac{\mathrm{d}r}{\mathrm{d}z} = \frac{v^r}{v^z}. \tag{21}$$

If we had included equation (5b) in the scheme then λ_0 would have been a triple root with the third solution giving $\mathrm{d}S = 0$ along the streamline (21).

At this point equations (17)-(21) may be written in a form more suitable for a numerical solution. Following Courant and Friedrichs (1967), (see also Sanders 1983, Daly and Marscher 1988 and Anderson 1985) we write the fluid 3-velocity components as

$$v^r = V \sin\Theta \qquad \text{and} \qquad v^z = V \cos\Theta \tag{22}$$

where Θ is the angle between the velocity vector of magnitude V and the symmetry axis (z-axis) of the jet. We also introduce the relativistic Mach angle, μ, defined by

$$\sin\mu = 1/M, \tag{23}$$

however, for the magnetic flows considered here it is more convenient to use a modified version of this, which is given by

$$\sin^2\xi = A \sin^2\mu. \tag{24}$$

We note from (18) that in order for the characteristics to be real (i.e. for the system to be hyperbolic) we must have $M^2 \geq A$ or equivalently $|\sin\xi| \leq 1$, and therefore the substitution (24) is valid for the purposes of the solution method described here. This is just the condition that the flow be supermagnetosonic in order to maintain a hyperbolic system. Substituting (22) and (24) into equations (17)-(21) produces the following compatibility equations,

$$\mathrm{d}p + \frac{1}{2}\mu \mathrm{d}H + w(\Gamma^2 - 1)\tan\xi \left[\left(\frac{1}{\cot\xi \pm \cot\Theta}\right) \mathrm{d}\ln r \pm \mathrm{d}\Theta\right] = 0 \tag{25}$$

holding along the C^+ and C^- curves

$$\frac{\mathrm{d}r}{\mathrm{d}z} = \tan(\Theta \pm \xi) \tag{26}$$

and

$$I \qquad \frac{A}{2(A-1)w} \mu \mathrm{d}H + \mathrm{d}\ln\Gamma = 0 \tag{27}$$

$$II \qquad \frac{A}{w}\mathrm{d}p + \mathrm{d}\ln\Gamma = 0 \tag{28}$$

holding along the streamline

$$\frac{\mathrm{d}r}{\mathrm{d}z} = \tan\Theta, \tag{29}$$

where $H = (h^\theta)^2$.

By combining equations (27) and (28) it is possible to obtain a generalization of the relativistic Bernoulli equation when a magnetic field is present;

$$p_*^{p_*/w}\Gamma = \text{constant along a streamline}, \tag{30}$$

where $p_* = p + \frac{1}{2}\mu H$ is the effective total pressure.

3. Junction conditions at an oblique shock front

If the ratio of the jet pressure to the external pressure is sufficiently high or low, then internal shocks will occur. Since the characteristic method cannot 'capture' shocks it is necessary to use a shock fitting scheme. For this we require the relations between fluid variables on either side of the shock region. These are given by the following jump conditions (Lichnerowicz 1967),

$$[\rho u^\alpha]\, N^\alpha = 0 \tag{31}$$

$$\left[T^{\alpha\beta}\right] N^\alpha = 0 \tag{32}$$

and

$$\left[u^\alpha h^\beta - u^\beta h^\alpha\right] N^\alpha = 0 \tag{33}$$

where $[Z]$ denotes the jump in the quantity Z across the shock and N_α are the components of the unit four-vector normal to the shock surface. We call ψ the angle between the shock normal and the positive z-direction (see figure 1), then the components of N_α are

$$N_\alpha = (0, \sin\psi, 0, \cos\psi). \tag{34}$$

The configurations considered in this paper are such that the magnetic field always acts transversely to the direction of propagation of the shock surface, i.e.

$$h^\alpha N_\alpha = 0. \tag{35}$$

Thus in our case, the system (31)-(33) reduces to the following,

$$\rho_u \Gamma_u v_{u\perp} = \rho_s \Gamma_s v_{s\perp} \tag{36}$$

$$w_u \Gamma_u^2 v_{u\perp} = w_s \Gamma_s^2 v_{s\perp} \tag{37}$$

$$w_u \Gamma_u^2 v_{u\perp}^2 + p_u + \frac{1}{2}\mu H_u = w_s \Gamma_s^2 v_{s\perp}^2 + p_s + \frac{1}{2}\mu H_s \tag{38}$$

$$w_u \Gamma_u^2 v_{u\perp} v_{u\parallel} = w_s \Gamma_s^2 v_{s\perp} v_{s\parallel} \tag{39}$$

and

$$h_u^\theta \Gamma_u v_{u\perp} = h_s^\theta \Gamma_s v_{s\perp} \tag{40}$$

where $v_\perp$ and $v_\parallel$ are the velocity components perpendicular and parallel to the shock surface, respectively. The unshocked values of the fluid variables (upstream of the shock) are indicated by the subscript u, while the subscript s is used for the shocked values. The component of fluid velocity parallel to the shock surface must be continuous across the shock as can be easily verified by combining equations (37) and (39). For a stable shock the normal component of velocity must instead decrease across it; so, as in Königl (1980), we introduce the quantity

$$\chi = \frac{v_{s\perp}}{v_{u\perp}} = \frac{\tan(\psi - \Theta_u)}{\tan(\psi - \Theta_s)} \leq 1 \tag{41}$$

which provides a measure of the shock strength .

For the purpose of numerical integration it is convenient to rewrite equations (36)-(40) such that the shocked values are expressed only in terms of the upstream values and the angle ψ. Assuming an ultra-relativistic (barotropic) equation of state, $p = (\gamma - 1)e$, we obtain a quadratic for χ, with solutions,

$$\chi = Y\left[1 \pm \sqrt{1 + \frac{(2-\gamma)\,\mu H_u}{Y\gamma\left(p_u + \frac{1}{2}\mu H_u\right)}}\right] \tag{42}$$

where

$$Y = \frac{\gamma\left(p_u + \frac{1}{2}\mu H_u\right)\left(\Gamma_u^2 v_{u\perp}^2 + 1\right)}{2w_u \Gamma_u^2 v_{u\perp}^2} \quad \text{and} \quad \Gamma_u^2 v_{u\perp}^2 = \frac{(\Gamma_u^2 - 1)(1 + \tan\psi \tan\Theta_u)^2}{(1 + \tan^2\psi)(1 + \tan^2\Theta_u)}.$$

From (42) we see that only the plus sign provides a physical solution, in which case,

$$\tan\Theta_s = \frac{\chi \tan\psi (1 + \tan\psi \tan\Theta_u) - (\tan\psi - \tan\Theta_u)}{\tan\psi (\tan\psi - \tan\Theta_u) + \chi (1 + \tan\psi \tan\Theta_u)} \tag{43}$$

$$\Gamma_s = \frac{\Gamma_u}{\sqrt{1 + \Gamma_u^2 v_{u\perp}^2 (1 - \chi^2)}} \tag{44}$$

$$h_s^\theta = \frac{h_u^\theta}{\chi}\sqrt{1 + \Gamma_u^2 v_{u\perp}^2 (1 - \chi^2)} \tag{45}$$

$$p_s = \left[1 + \Gamma_u^2 v_{u\perp}^2 (1 - \chi^2)\right]\left[\frac{p_u}{\chi} - \frac{(\gamma - 1)(1 - \chi)}{\gamma \chi^2}\mu H_u\right]. \tag{46}$$

Given the conditions of the flow upstream of the shock it is clear that once ψ is known all quantities on the downstream side can be found. However, to determine ψ, information from the downstream side of the shock must be provided. This information is obtained via the $\mathcal{C}^-$ or $\mathcal{C}^+$ curves, depending on whether the shock is incident or reflected. Further details and a description of the numerical procedure adopted are given in the next section.

Figures 2 and 3 show solutions of the jump conditions (42)-(46) when $\gamma = 4/3$. The parts of the figures show logarithmic contour plots of (a) the downstream Mach number and (b) the thermal pressure jump, p_s/p_u, for the upstream Mach number between 1 and 50 and the shock angle $\delta = \psi - \Theta_u$ between 0^o and 90^o. In the case of figure 2 no magnetic field is present (hydrodynamical shocks), while for figure 3 the upstream thermal and magnetic pressures are equal (i.e. $p_u = \frac{1}{2}\mu H_u$). The magnetic field jump, h_s^θ/h_u^θ, is qualitatively identical to the pressure jump.

Since we are using the method of characteristics it is necessary for the flow to be supermagnetosonic (i.e. $M^2 > A$) everywhere. The shaded region on the left of the figures is where this condition is not satisfied. Apart from slightly supersonic upstream flows the transition from super to submagnetosonic flows occurs at almost constant values of shock angle; these being $\delta = 30^o$ and $\delta = 45^o$ for figures 2 and

3 respectively. It is interesting to note that once the upstream flow is moderately supersonic, e.g. $M \geq 4$, then the downstream Mach number is essentially only a function of the shock angle δ. Unless the shocks are quite oblique the bulk fluid velocity can be reduced very substantially. For example, a fluid with an initial Mach number of 20 passing through a shock with $\delta = 60^o$ has a final Mach number of ~ 2.5, if no magnetic field is present. For equal thermal and magnetic pressures the final Mach number is higher at ~ 3.5 (and is increasing for increasing field strength), nevertheless it is still substantially reduced. This does not, of course, take account of jet expansion, which, for a supersonic flow, would increase the velocity. However if the jet is well collimated, at least near the nozzel as we assume, then no such speed up would occur. This suggests that in order for a jet to form and progress into the surrounding medium then, close to the nozzel, either no or very weak shocks are present, or they are very oblique. A very small number (two or three) of moderately perpendicular shocks ($\delta < 60^o$) would rapidly disrupt the progress of the jet due to the flow becoming subsonic and turbulent. For an increasing magnetic field the shock strength (as measured by the ratio p_s/p_u) decreases. This is due to a stiffening of the jet fluid since it behaves with an effective adiabatic index $\gamma \to 2$ as the field increases. This is because the magnetoacoustic and Alfvén wave speeds approach the velocity of light. Then it becomes increasingly difficult to produce strong shocks (see De Hoffman and Teller 1950; Kennel and Coroniti 1984; Appl and Camenzind 1988). Thus the toroidal magnetic field could have a number of vital roles in the production and propagation of the jet. First, the toroidal field helps to form the nozzel itself; second, it can reduce the tendency of nozzel breakup due to fluid instabilities; third, a strong toroidal field can inhibit the formation of strong shocks, which could otherwise cause a rapid termination of the jet. Since the toroidal field strength appears to be a crucial factor, any significant asymmetries in the field configuration can easily lead to one-sided sources (Benford, 1987).

When $\chi > 1$ the fluid velocity component normal to the shock front is not supermagnetosonic and therefore a shock cannot form. This condition is indicated by the shaded region on the right-hand-side of figures 2 and 3. The boundary of the region at $\chi = 1$ corresponds to the solution $\log(p_s/p_u) = 0$.

4. Numerical solution method

The system (25)-(29) is a set of seven equations which must be solved for the unknown variables p, Θ, H and Γ on a grid constructed from characteristic curves, i.e. the grid itself must be obtained as part of the solution. We will outline the salient features of the numerical procedure adopted to do this since, although the techniques are well known in engineering fluid dynamics, they may not be familiar to many astrophysicists. Moreover there are a number of novel features in our problem which make the integration procedure somewhat non-standard, in particular the presence of the magnetic field and the fact that we will integrate along the streamlines in addition to the forward and backward characteristic curves.

The basic techniques described here are similar to those used in jet nozzel design (see e.g. Anderson 1982, 1985 or Owczarek 1964) except that in this case the outer boundary is a free surface rather than a wall. There are primarily four different types of grid point; (i) an internal point, (ii) an axis point, (iii) a free surface point and (iv) a shock point, shown in figures 4(a)-(d) respectively. We will consider the treatment of each type of point in turn.

(i) Internal points:

Since the system is hyperbolic the equations are integrated in the z-direction (taken to be a pseudo time) from an initial r =constant Cauchy slice. Consider the situation shown in figure 4(a) in which the filled circles represent grid points at which the data is known. The goal is to use this data to compute not only the unknowns at the new grid points (open circle), but also the positions of such points. This requires the use of an iterative procedure. First, the position of point 3 in figure 4(a) is determined by the intersection of the $\mathcal{C}^+$ and $\mathcal{C}^-$ characteristic curves from points 1 and 2 respectively, the slopes of which are given by equation (26). We will approximate the characteristic curves between adjacent grid points by straight lines. Referring to figure 4(a), it is also necessary for the streamline to pass through grid point 3, and therefore initial data must be interpolated from points 1 and 2 to a point 4 where the base of the streamline intersects a line joining 1 and 2. A simple linear interpolation scheme is adequate for this purpose. Thus, at the general point 3 all seven equations need to be solved together iteratively to find p_3, Θ_3, H_3, Γ_3, r_3, z_3 and r_4 where the subscript refers to the grid point numbers shown in figure 4(a).

The equations (25)-(29) are finite-differenced in a very simple way, e.g. from (26) the $\mathcal{C}^+$ curve from 1 to 3 is written as,

$$r_3 - r_1 = \frac{1}{2}[\tan(\Theta_3 + \xi_3) + \tan(\Theta_1 + \xi_1)](z_3 - z_1), \tag{47}$$

and from (25) the equation holding along this curve is written as,

$$(p_3 - p_1) + \frac{1}{2}\mu(H_3 - H_1) + \frac{1}{2}\left[\frac{w_3(\Gamma_3^2 - 1)\tan\xi_3}{\cot\xi_3 + \cot\Theta_3} + \frac{w_1(\Gamma_1^2 - 1)\tan\xi_1}{\cot\xi_1 + \cot\Theta_1}\right]\ln\left(\frac{r_3}{r_1}\right)$$
$$+ \frac{1}{2}[w_3(\Gamma_3^2 - 1)\tan\xi_3 + w_1(\Gamma_1^2 - 1)\tan\xi_1](\Theta_3 - \Theta_1) = 0. \tag{48}$$

The other equations are differenced in a similar way. With initial estimates for the unknowns the coupled non-linear algebraic equations can be solved at each grid point using the MINPACK iteration routine HYBRD1; this has proved to be an efficient solution method.

(ii) Axis points:

The jets are axisymmetric and therefore the z-axis is a coordinate singularity and special treatment is required for equation (25). There are two possible situations to consider; (a) when the data at the axis point is known and is being used to propagate data forward, or (b) when the data is to be computed on the axis point. Figure 4(b) shows both situations, which occur alternately as we integrate in the z-direction. In case (a) the equation holding along the $\mathcal{C}^+$ characteristic curve from point 1 must be modified. Consider the term $\mathrm{d}\ln r/(\cot\xi + \cot\Theta)$ in the limit $r \to 0$. We have that $\Theta \to 0$ also since at $r = 0$ the flow must be along the axis. Therefore,

$$\lim_{r,\Theta\to 0}\left(\frac{1}{\cot\xi + \cot\Theta}\right)\frac{\mathrm{d}r}{r} = \lim_{r,\Theta\to 0}\tan\Theta\frac{\mathrm{d}r}{r} = \lim_{r,\Theta\to 0}\frac{\Theta}{r}\mathrm{d}r = \frac{\mathrm{d}\Theta}{\mathrm{d}r}\mathrm{d}r = \mathrm{d}\Theta. \tag{49}$$

With this modification grid point 3 is treated in exactly the same way as an ordinary internal point described above. For case (b) (grid point 5 in figure 4(b)), due to axisymmetry not all seven equations are required. The position of the grid point is $r = 0$ with the z value to be obtained from the intersection of the $\mathcal{C}^-$ curve with the axis. By symmetry the $\mathcal{C}^+$ equation is the mirror image and so can be discarded. In addition the streamline itself is known, it is simply the z-axis, thus $\Theta = 0$ which implies that equation (29) can also be discarded. Another condition on the axis concerns the magnetic field component h^θ, which, in order to be non-singular, must vanish.

Therefore equation (27) is discarded and $H = 0$ on the axis may be used to simplify the remaining equations. Then the unknown quantities at grid point 5 are p_5, Γ_5 and z_5, and the equations used are the $\mathcal{C}^-$ curve from (26), its compatibility equation from (25), which must be modified using the limit shown in (49), and equation (28) holding along the streamline between points 1 and 5.

(iii) Boundary points:

The outer boundary is a free surface where the pressure of the external medium is specified. In principle it is possible to specify the flow angle, Θ, rather than the pressure, so that the jet shape can be customized, leading to a particular behaviour of the external pressure gradient. This was done by Wilson (1987a), however here we will use only specified external pressure values.

The grid structure at the boundary is shown in figure 4(c) where the data is known at points 1 and 2 and the boundary values of Θ, H, Γ and position r, z at point 3 are to be determined. Noting that the jet boundary, curve 2 to 3, is a streamline the equations required are the $\mathcal{C}^+$ curve from 1 to 3 and its compatibility equation (from (26) and (25) respectively) and the streamline equations (27)-(29). Again an iterative procedure is used.

(iv) Shock points:

As discussed in the previous section, if the ratio of jet pressure to external pressure is sufficiently high or low then internal shocks will occur. There are two problems to consider in the numerical treatment of these shocks; firstly their detection and secondly their propagation through the characteristic grid.

A shock is indicated when two characteristics of the same family, say $\mathcal{C}^+$, intersect. The position of the shock point is easily determined from the slopes of the characteristic curves. At the shock point it is then necessary to solve the relativistic Rankine-Hugoniot relations (42)-(46) along with the characteristic and compatibility equations. The shock detection and fitting procedure is essentially the same as that used to propagate a previously inserted shock point, which we now describe.

Once a shock point has been detected it must be propagated throughout the characteristic grid. The following procedure is based on that described by Moe and Troesch (1960) and Illingworth (1953) for their Newtonian jet calculations.

Consider the situation shown in figure 4(d) where 1, 2 and 3 are known data points

and 2 is a shock point (which is double valued in that it carries a set of unshocked and shocked values of the fluid variables). First point 4 is obtained from 1 and the unshocked side of 2 using the standard procedure for an internal point, as described above. From the value of the shock angle, $\delta_2 = (\psi - \Theta_u)_2$, at 2, point 5 may be determined as the intersection of the shock path with the $\mathcal{C}^+$ characteristic curve 1 to 4. At 5 the unshocked values Θ_u, Γ_u, p_u and H_u may be determined by interpolation between 1 and 4. To find the shocked values of the quantities and the new shock angle it is necessary to solve the jump conditions (42)-(46) at 5 along with the $\mathcal{C}^-$ characteristic and compatibility equations extending back from point 5, with base values at point 6 interpolated from points 2 (shocked side) and 3. From equations (25) and (26) we have that these last two equations are:

$$r_5 - r_6 = \frac{1}{2}[\tan(\Theta_s - \xi_s) + \tan(\Theta_6 - \xi_6)](z_5 - z_6), \tag{50}$$

and

$$(p_s - p_6) + \frac{1}{2}\mu(H_s - H_6) + \frac{1}{2}\left[\frac{w_s(\Gamma_s^2 - 1)\tan\xi_s}{\cot\xi_s - \cot\Theta_s} + \frac{w_6(\Gamma_6^2 - 1)\tan\xi_6}{\cot\xi_6 - \cot\Theta_6}\right]\ln\left(\frac{r_s}{r_6}\right)$$
$$- \frac{1}{2}[w_s(\Gamma_s^2 - 1)\tan\xi_s + w_6(\Gamma_6^2 - 1)\tan\xi_6](\Theta_s - \Theta_6) = 0. \tag{51}$$

Once again this is an iterative procedure to find the shocked values Θ_s, Γ_s, p_s and H_s, the new shock angle $\delta_5 = (\psi - \Theta_u)_5$, and the foot of the interpolated $\mathcal{C}^-$ characteristic curve, r_6, z_6; a total of seven equations for seven unknowns.

5. Results of calculations

In a constant external medium our jet models are characterized by three parameters; α, β and M_{jet} where

$$\alpha = \left(\frac{\text{pressure of external medium at base of jet}}{\text{initial pressure at base of jet}}\right)^{1/2} = \left(\frac{p_{ext}}{p_{jet}}\right)^{1/2}$$

$$\beta = \left(\frac{\text{largest magnetic pressure at base of jet}}{\text{initial pressure at base of jet}}\right) = \left(\frac{\frac{1}{2}\mu H_{max}}{p_{jet}}\right)$$

M_{jet} = initial Mach number of jet flow.

Note that our β is the reciprocal of the usual plasma β. For all the models shown in this paper an ultra-relativistic equation of state, $p = (\gamma - 1)e$, with adiabatic index $\gamma = 4/3$, is used. The initial conditions at the nozzel entrance are shown in figure 5. In practise the step function at the boundary is modelled by three grid points. Given the pressure and magnetic field values on the boundary it is possible to obtain the Lorentz factor there by using the Bernoulli relation (30) and assuming the streamline constant is approximately the same for adjacent points. The toroidal field configuration is given by

$$H = H_{max}(r/r_{patch})^2 \qquad \text{if} \qquad r < r_{patch}$$
$$H = H_{max}(r_{patch}/r)^2 \qquad \text{if} \qquad r \geq r_{patch}$$

where usually $r_{patch} = 0.98 r_{jet}$. This configuration is similar to that used by Lind *et al* (1989) in their dynamical simulations. For a typical case the initial data line is modelled using $\sim$ 80 grid points. As the calculation proceeds grid points may be added if the distance between adjacent points exceeds a certain value (with linear interpolation to the new points) or deleted if they are too close. This facility is vital for the success of the characteristic method. A complete calculation may consist of more than $\sim 10^5$ data points.

5.1. Tests of the code

In order to check that the code is performing as expected we have used the analytic expressions obtained by Daly and Marscher (1988) for the maximum radius, r_{max}, and length-scale, z_{max} (the distance from the nozzel entrance to the next minimum radius, see figure 1 of Daly and Marscher) of a non-magnetic supersonic jet propagating in a uniform pressure medium. They state that

$$\frac{r_{max}}{r_{jet}} \sim 1 + 1.9\left(\frac{1-\sqrt{\alpha}}{2\sqrt{\alpha}-1}\right) \tag{52}$$

and

$$\frac{z_{max}}{r_{jet}} \sim 3.3\left(\frac{\Gamma_{jet}}{\alpha^2}\right). \tag{53}$$

These expressions have been obtained by taking small angle expansions in the two-dimensional (planar) characteristic equations (Daly and Marscher, 1988). They are accurate for large Γ_{jet} and α close to one.

Taking $r_{jet} = 1$ and $\Gamma_{jet} = 7.14$ (corresponding to $M_{jet} = 10$) we have computed r_{max} and z_{max} for various values of α. As can be seen from Table 1 the numerical and theoretical values are close for $\alpha \sim 1$, but diverge as the pressure ratio becomes larger, as would be expected. Some additional discrepancy occurs because we are simulating axisymmetric jets rather than planar ones. From expression (49) we see that on the z-axis there is a factor of 2 difference in equation (11d) of Daly and Marscher between planar and axisymmetric jets. Their expression (23) for the minimum pressure is therefore invalid in our case, and indeed, we obtain significantly lower values of the minimum pressure. This would aid collimation, leading to lower values of r_{max} and z_{max}, which is consistent with our results.

A consistency check on the code is possible by making use of the Bernoulli equation (30) along the z-axis; which is a streamline. The percentage deviation from a constant value for expression (30) is shown in figure 6 for two jets with $1/\alpha^2 = 1.2$, $\beta = 0$ (solid lines) and $1/\alpha^2 = 1.2$, $\beta = 1$ (broken lines), both of which have either 40 or 80 grid points across the nozzel entrance. No shocks occur in these jets. It can be seen that the Bernoulli equation is satisfied to $< 1\%$ in the case of 40 points and $< 0.5\%$ in the case of 80 points. Thus the discretization error can be reduced by increasing the number of points in the jet. Some numerical experiments have indicated that the error behaves in a first-order way, i.e. doubling the number of points across the nozzel reduces the percentage deviation by approximately half.

5.2. Collimation via a toroidal magnetic field - constant external pressure

For a first application of our code we will study the effect of an increasingly strong toroidal magnetic field on the structure of an underexpanded jet propagating into an external medium of uniform pressure. As mentioned previously in section 3, such a magnetic field could be responsible for the initial creation, stability and continued propagation of the jet.

There are four characteristic velocities associated with the flows under consideration here. These are;

(i) sound velocity	$v_S = 1/\sqrt{3}$
(ii) Alfvén wave velocity	$v_A = [\beta/(2+\beta)]^{1/2}$
(iii) fluid bulk velocity	$v_{jet} = [M_{jet}^2/(2+M_{jet}^2)]^{1/2}$

(iv) fast magnetosonic velocity $v_M = [(c_S^2 + \Gamma_S^2 c_A^2)/(1 + c_S^2 + \Gamma_S^2 c_A^2)]^{1/2}$.

All of these quantities can also be written in a quasi-Newtonian form (they can approach infinity and there is some formal similarity with the corresponding Newtonian equations when such quantities are used, see Königl 1980), i.e.

(i) sound velocity $c_S = 1/\sqrt{2}$
(ii) Alfvén wave velocity $c_A = (\beta/2)^{1/2}$
(iii) fluid bulk velocity $c_{jet} = M_{jet}/\sqrt{2}$
(iv) fast magnetosonic velocity $c_M = (c_S^2 + \Gamma_S^2 c_A^2)^{1/2}$.

Note that c_M is a particular case of equation (45) in Königl (1980). Of course, the quasi-Newtonian quantities are not physical in the special relativity regime. From these expressions it can be seen that for a flow to be super-Alfvénic only a modest Mach number is required, even if the magnetic field is extremely strong; i.e. $M_{jet}^2 \geq \beta$. Thus if $\beta = 4$ we require only that $M_{jet} \geq 2$. The relativistic Alfvén Mach number can be written as $M_A = c_A/c_S = \sqrt{\beta}$. For our simulations, typically $M_{jet} \geq 10$, so the jets are always highly supermagnetosonic, at least close to the nozzel.

Initially we take fixed parameter values of $1/\alpha^2 = 1.5$ and $M_{jet} = 10$. Then β is varied from $\beta = 0$ (purely hydrodynamical) to $\beta = 2$ (dominant magnetic field). In these cases the pressure discontinuity is sufficiently weak that the jets do not produce shocks, even when the magnetic field is zero. The results of the calculations are shown in figures 7(a)-(c). In 7(a) the jet radius is plotted as a function of distance along the z-axis. Even when no magnetic field is present the jet is well collimated, due to the existence of the constant pressure external medium. The maximum radial expansion is only 20% larger than the starting radius. In addition, it can be seen that a small toroidal field can substantially reduce the jet expansion. For $\beta > 0.5$ the jet is severely pinched and it contracts. The least variation in the jet boundary shape is produced when $\beta \sim 0.5$. As β increases the jet oscillations become more frequent and the jet boundary shape more periodic. Thus portions of a jet with a strong toroidal magnetic field component could exhibit several very periodic bright features (e.g. knots), particularly since at such points the pressure on the axis is greatly enhanced and radio emission is likely to follow the fluid pressure. This pinch effect is clearly seen in figure 7(b) which plots the logarithm of the jet pressure on the z-axis.

The external pressure is constant at $p_{ext} = 1$. However, figure 7(c) shows that the bulk fluid velocity is reduced as the magnetic field strength increases and this would then reduce the relativistic beaming. The high pressure regions work against collimation, but this is more than compensated for by the pinching effect of the toroidal field. In figure 8 we show contour plots for, (a) the logarithm of the thermal pressure; (b) the logarithm of the Mach number, and (c) the magnetic pressure, for the case of $\beta = 2$. These plots clearly show the very periodic formation of islands of slowly moving, high pressure gas pinched by an intense magnetic field.

From the results of these simulations the following comments can be made about the effects of the toroidal magnetic field. When no field is present the jet can have very large pressure and velocity changes along its length. From figure 7(a) when $\beta = 0$ the maximum z-axis pressure is approximately equal to that at the nozzel entrance. On the other hand, the maximum Mach number (or equivalently Γ) can increase by a factor of two. These variations decrease as β increases. The least variation in jet pressure and velocity occurs approximately for $\beta = 0.5$. Above this value the jet radius decreases. When β is large the thermal pressure on the z-axis can be much larger than the external pressure without decollimation occurring. Thus bright knots could be associated with a locally strong toroidal magnetic field. However, if a strong longitudinal magnetic field were present, this could work against collimation (Kössl *et al* 1990c).

5.3. Collimation via a toroidal magnetic field - decreasing external pressure

A more realistic environment for astrophysical jets is one of an external medium with varying pressure distribution. X-ray data seem to indicate a general power-law fall-off in pressure with distance from the jet source, at least for elliptical galaxies (Schreier *et al* 1982). Here we will investigate the effects of the toroidal magnetic field on the structure of the jet when it propagates into an external medium with a pressure distribution given by,

$$p'(z) = \frac{p_{ext}}{[1 + (z/z_{core})^n]^{m/n}}. \qquad (54)$$

This is similar to that used by Wilson and Falle (1985). Within the core radius, z_{core}, the external pressure is roughly constant, but outside it has a power-law fall-off as $p' \propto z^{-m}$. Typically $1 \leq m \leq 2$ and $z_{core} \sim$ a few jet radii.

In this investigation the values of the parameters describing the underexpanded jets of the previous subsection will again be used, but this time with the external pressure given by (54). We will first take $z_{core} = 15$, $n = 4$ and $m = 2$. Then the external pressure drops sufficiently rapidly that a pure hydrodynamical jet will undergo free expansion (Wilson and Falle 1985). The range of β is again taken to be from $\beta = 0$ to $\beta = 2$. Figures 9(a)-(d) shows the results of the simulations. Since the structures of these jets are much less periodic than those in a constant pressure external medium, we have allowed them to propagate much further.

As expected the $\beta = 0$ jet expands continuously, giving rise to a region of extremely low pressure and high velocity gas. This gas is quite strongly shocked, which brings it into near pressure equilibrium with the external medium (the pressure distribution of the external medium is shown as the thick solid line in 9(b)). There is no evidence of recollimation of the jet. In fact, from figure 9(a), it can be seen that no significant recollimation occurs for any value of β used here. This is because as the jet expands and the external pressure decreases the magnetic field strength is reduced and becomes less effective at pinching the plasma (see figure 9(d)). The magnetic field, however, does prevent shock formation and keeps the jet pressure substantially higher than that of the external medium. Moreover when the toroidal field is very strong ($\beta > 2$) pressure perturbations at the nozzel are efficiently propagated downstream to produce a number of peaks in the z-axis pressure. Such jets would appear with bright knots of increasing separation (and decreasing brightness). In figure 10(a)-(c) we show contours of (a) the logarithm of pressure, (b) logarithm of Mach number and (c) magnetic field strength for the $\beta = 2$ model.

We have repeated a similar experiment to the above, but this time with $z_{core} = 15$, $n = 4$ and $m = 1$, so that the external pressure drops as $p' \propto z^{-1}$. In this case, as can be seen from figure 11(a)-(d), the periodic structure seen in the p_{ext} = constant models reappears, particularly as β increases. Again, however, the jets continue to expand, although this time reconfinement shoulders do appear even in the $\beta = 0$ model. When $\beta = 0$ the jet pressure oscillates continuously about the external pressure value. For $\beta > 0$, as in the previous cases, the jet pressure is always much higher than the external pressure. In figure 12(a)-(c) we show contour plots of (a) the logarithm of pressure, (b) logarithm of Mach number and (c) magnetic field strength for the $\beta = 2$ model.

6. Conclusions and Discussion

The previous results show aspects of steady relativistic MHD flows which may be of direct relevance to astrophysical jets, in particular compact radio jets which exhibit superluminal motion (Blandford and Königl 1979). No attempt has been made to model any specific observed jet since the physics we have used is far too simplified for detailed comparisons with observations. We can, however, make a number of general comments.

An important dynamical effect of the magnetic field is in reducing the tendency for strong shock formation in the flow, however, large pressure peaks still form when the jet reconfines. These high pressure regions coincide with large toroidal magnetic field strengths and low bulk fluid velocities. As such they would be identified with the bright knots in a jet, but, while the high pressure and magnetic field enhances synchrotron emission, beaming is reduced due to a lower Lorentz factor. The actual brightness of the knots in a synthesised radio map requires a correct treatment of the synchrotron radiation process taking into account beaming and line-of-sight effects (see e.g. Matthews and Scheuer 1990a,b). It is also of interest to note that while the toroidal field can keep the jet pressure well above that of the external medium, it cannot stop the radial expansion of the jet when the external pressure drops. The rate of radial expansion, however, is reduced with increasing toroidal field strength.

The constant external pressure scenario is not a realistic one for astrophysical jets, but it illustrates an important phenomenon which persists when the external medium has varying pressure. As the toroidal field strength increases the jet structure becomes more and more periodic. In addition reconfinement and reexpansion of the jet occurs on a shorter and shorter length scale. This is due to the dynamics being taken over by the magnetic field, which has as its characteristic velocity the Alfvén wave speed. Then as the magnetic field strength increases this velocity approaches light speed.

When the external pressure varies as $p' \propto z^{-2}$ no periodic structures appear in the jet in the absence of a magnetic field. In this case the jet ultimately reduces to a stream of gas with a very high Mach number (> 40) in approximate pressure equilibrium with its surroundings and with an almost constant opening angle. This portion of the jet is unlikely to be visible. Moreover there are no significant pressure enhancements anywhere, even close to the nozzel (see figure 9). Therefore none of this jet may be

visible. As the magnetic field strength is increased the pressure perturbation, which is formed close to the nozzel by the pinching effect of the field, is propagated downstream with greater and greater efficiency . The first pressure peak is always the largest and can be identified with the bright core of the jet. Subsequent pressure peaks could give rise to knots which probably decrease in brightness and have an increasing inter-knot distance moving out along the jet axis (see figure 9(b)). For a fixed pressure distribution of the external medium the knots would increase in brightness and decrease in separation as the toroidal field strength increases. Moreover, additional knots could appear where none existed before.

If the external pressure $p' \propto z^{-1}$ some periodicity of the jet structure returns, particularly when the magnetic field strength is large. From figure 11, however, it is seen that there are many pressure peaks when $\beta = 2$. This would give rise to a large number of bright knots, and since there are no observations of this type it is unlikely that a combination of $p' \propto z^{-1}$ and $\beta \geq 2$ occurs in practice. The best parameters for observed jets seems to be around $p' \propto z^{-2}$ and $\beta \sim 2$. In any case it could be possible to arrange the number, positions and brightness of knots in a jet using a simple combination of the external pressure distribution and the toroidal field strength in much the same way that Falle and Wilson (1985) did with the external pressure distribution to model specific knots in M87. This will be investigated in future work.

Acknowledgments

We are very grateful to John Miller for reading the manuscript and making helpful suggestions for its improvement. This work was undertaken at SISSA, Trieste; Dipartimento di Fisica, Padova and the Center for Relativity, Austin, Texas. We thank all of these institutions for their hospitality. MRD acknowledges the receipt of a SERC/NATO postdoctoral fellowship. Some of the computations in this paper were performed using the Cray Y-MP8/864 at the Center for High Performance Computing, University of Texas System, with Cray time supported by a Cray University Research grant to Richard Matzner. The Ministero Italiano per l'Università e la Ricerca Scientifica e Tecnologica is acknowledged for financial support. This work was supported in part by NSF Grant No. PHY-8806567.

References

Anderson, J.D. (1982) *Modern Compressible Flow: With Historical Perspective,* McGraw-Hill

Anderson, J.D. (1985) *Fundamentals of Aerodynamics,* McGraw-Hill

Anile, A.M. and Pennisi, S. (1985) *Ann. Inst. Henri Poincaré* **46** 27

Anile, A.M. (1989) *Relativistic Fluids and Magneto-fluids with Applications in Astrophysics and Plasma Physics,* Cambridge University Press

Appl, S. and Camenzind, M. (1988) *Astron. Astrophys.* **206** 258

Benford, G. (1987) in *Astrophysical Jets and their Engines,* ed. W. Kundt, D. Reidel Publishing, p197

Blandford, R.D. and Königl, A. (1979) *Astrophys. J.* **232** 34

Courant, R. and Friedrichs, K.O. (1948) *Supersonic Flows and Shockwaves,* Springer-Verlag

Daly, R.A. and Marscher, A.P. (1988) *Astrophys. J.* **334** 539

De Hoffman, F. and Teller, E. (1950) *Phys. Rev.* **80** 692

Dubal, M.R. (1991) *Comp. Phys. Commun.* **64** 221

Falle, S.A.E.G. and Wilson, M.J. (1985) *M.N.R.A.S* **216** 79

Falle, S.A.E.G. (1991) *M.N.R.A.S* **250** 581

Falle, S.A.E.G. (1987) in *Astrophysical Jets and their Engines* ed. W. Kundt, Reidel p151

Ferrari, A., Trussoni, E. and Zaninetti, L. (1981) *M.N.R.A.S.* **196** 1051

Illingworth, C.R. (1953) in *Modern Developments in Fluid Dynamics: High Speed Flow Vol. 1* ed. L. Howarth, Oxford University Press

Kennel, C.F. and Coroniti, F.V. (1984) *Astrophys. J.* **283** 694

Königl, A. (1980) *Phys. Fluid* **23** 1083

Kössl, D., Müller, E. and Hillebrandt, W. (1990a) *Astron. Astrophys.* **229** 378

Kössl, D., Müller, E. and Hillebrandt, W. (1990b) *Astron. Astrophys.* **229** 397

Kössl, D., Müller, E. and Hillebrandt, W. (1990c) *Astron. Astrophys.* **229** 401

Lichnerowicz, A. (1967) *Relativistic Hydrodynamics and Magnetohydrodynamics,* Benjamin, New York

Lind, K.R., Payne, D.G., Meier, D.L. and Blandford, R.D. (1989) *Astrophys. J.* **344** 89

Matthews, A.P. and Scheuer, P.A.G. (1990a) *M.N.R.A.S.* **242** 616

Matthews, A.P. and Scheuer, P.A.G. (1990b) *M.N.R.A.S.* **242** 623

Moe, M.M. and Troesch, B.A. (1960) *A.R.S.* **30** 487

Norman, M.L. and Winkler, K-H.A. (1984) in *Astrophysical Radiation Hydrodynamics,* eds. K-H.A. Winkler and M.L. Norman, D. Reidel Publishing

Owczarek, J.A. (1964) *Fundamentals of Gas Dynamics,* Scraton, International Textbook Co.

Sanders, R.H. (1983) *Astrophys. J.* **266** 75

Schreier, E.J., Gorenstein, P. and Feigelson, E.D. (1982) *Astrophys. J.* **261** 42

Sloan, J.H. and Smarr, L.L. (1987) in *Numerical Astrophysics* eds. J.M. Centrella, J. LeBlanc and R. Bowers, Jones and Bartlett, Boston

Wardle, J.F.C. and Potash, R.I. (1982) in *Proc. of IAU Symp. no. 97,* D. Reidel Publishing

Wilson, M.J. and Falle, S.A.E.G. (1985) *M.N.R.A.S* **216** 971

Wilson, M.J. (1984) *M.N.R.A.S* **209** 923

Wilson, M.J. (1987a) *M.N.R.A.S* **224** 155

Wilson, M.J. (1987b) *M.N.R.A.S* **226** 447

Zensus, J.A. and Pearson, T.J. (1987) *Superluminal Radio Sources,* Cambridge University Press

Tables and table captions

Table 1. Test of the code using the expressions for r_{max} and z_{max} given by Daly and Marscher (1988), denoted by D-M. Here $M_{jet} = 10$ and $\beta = 0$.

$1/\alpha^2$	r_{max} D-M	r_{max} Code	Diff %	z_{max} D-M	z_{max} Code	Diff %
1.1	1.0469	1.0393	0.73	25.923	25.425	1.92
1.3	1.1382	1.1137	2.15	30.637	27.450	10.40
1.5	1.2269	1.1841	3.49	35.350	30.705	13.14
2.0	1.4434	1.3462	6.73	47.133	38.433	18.45

Figure captions

Figure 1. Flow geometry at an incident oblique shock. See the text for details.

Figure 2. Logarithmic contour plots of (a) the post-shock Mach number and (b) the pressure jump for a range of upstream Mach numbers and shock angles when $\gamma = 4/3$. In this case no magnetic field is present. The shaded area on the left denotes the region where the characteristics are no longer real, i.e. $M^2 \leq A$, and is therefore not accessible using our numerical method. The shaded region on the right is where $\chi > 1$ and so does not correspond to shock solutions.

Figure 3. Same as figure 2 except that the upstream thermal and magnetic pressures are equal.

Figure 4. Calculation of data at the four different types of grid point occurring during the integration. The filled black areas denote points at which the data is known, open areas are points at which data is to be determined. (a) Calculation of data at an internal point 3. $\mathcal{C}^{\pm}$ are the forward and backward characteristics from point 3 and S is the streamline passing through 3. The foot of the streamline is at point 4. (b) Computation of axis points. Data points 3 and 5 require special treatment due to the axis singularity. (c) Computation of jet boundary points. The streamline B $(2 \rightarrow 3)$ is the jet's surface. (d) Propagation of the known shock point 2 (shown as a black square) through the grid. Point 5 is determined using the shock angle $\delta = \psi - \theta_u$ at 2. The curve $3 \rightarrow 5$ is an interpolated backward characteristic from the new shock point (white square).

Figure 5. Input conditions at base of jet ($z = 0$), showing the radial profiles of the thermal pressure, Lorentz factor and H.

Figure 6. Consistency check on the code. The Bernoulli equation (30) is evaluated along the z-axis for $1/\alpha^2 = 1.2$ with $\beta = 0$ (solid lines) and $\beta = 1$ (broken lines) when 40 or 80 grid points are placed along the nozzel entrance. The inconsistency behaves in a first-order way.

Figure 7. Results for a jet with $1/\alpha^2 = 1.5$ and $M_{jet} = 10$ for various values of β propagating into a constant pressure external medium: (a) Suppression of the radial

expansion of the jet due to an increasingly strong toroidal magnetic field. The values of β are denoted by: $\beta = 0$ (solid line); $\beta = 0.25$ (short dashed line); $\beta = 0.5$ (long dash-short dash line); $\beta = 1$ (dash-dot line); $\beta = 2$ (dotted line): (b) Variation of the thermal pressure on the jet axis and, (c) variation of the Mach number on the jet axis. In (b) and (c), for clarity, only the values $\beta = 0$, $\beta = 0.5$ and $\beta = 2$ are shown.

Figure 8. Contours of (a) logarithm of the thermal pressure, (b) logarithm of the Mach number, and (c) the toroidal magnetic field strength for the jet with $\beta = 2$. High values are denoted by the darkest regions and low values by the white regions (scaled between the maximum and minimum values of the quantity within the jet). Note that these figures have been greatly expanded in the radial direction. The initial jet radius is $r_{jet} = 1$ while the jet length is $z \approx 100$.

Figure 9. Results for a jet with $1/\alpha^2 = 1.5$ and $M_{jet} = 10$ for various values of β with the external pressure, p', given by (54). Here $n = 4$ and $m = 2$ so that $p' \propto z^{-2}$. Values of β are as indicated in figure 7.: (a) Suppression of the radial expansion of the jet due to an increasingly strong toroidal magnetic field. (b) Variation of the thermal pressure on the jet axis (p' denoted by the thick solid line), (c) variation of the Mach number on the jet axis and (d) the decay of the magnetic field on the jet boundary.

Figure 10. Contours of (a) logarithm of the thermal pressure, (b) logarithm of the Mach number, and (c) the toroidal magnetic field strength for the jet of figure 9 with $\beta = 2$. Values are scaled as in figure 8 and again the radial direction has been greatly expanded. Here $r_{jet} = 1$ and length $z \approx 250$.

Figure 11. Results for a jet with $1/\alpha^2 = 1.5$ and $M_{jet} = 10$ for various values of β with the external pressure, p', given by (54). Here $n = 4$ and $m = 1$ so that $p' \propto z^{-1}$: (a) Suppression of the radial expansion of the jet due to an increasingly strong toroidal magnetic field. Values of β are as indicated in figure 7. (b) Variation of the thermal pressure on the jet axis (p' denoted by the thick solid line), (c) variation of the Mach number on the jet axis and (d) the decay of the magnetic field on the jet boundary.

Figure 12. Contours of (a) logarithm of the thermal pressure, (b) logarithm of the Mach number, and (c) the toroidal magnetic field strength for the jet of figure 11 with

$\beta = 2$. Values are scaled as in figure 8 and again the radial direction has been greatly expanded. Here $r_{jet} = 1$ and length $z \approx 250$.

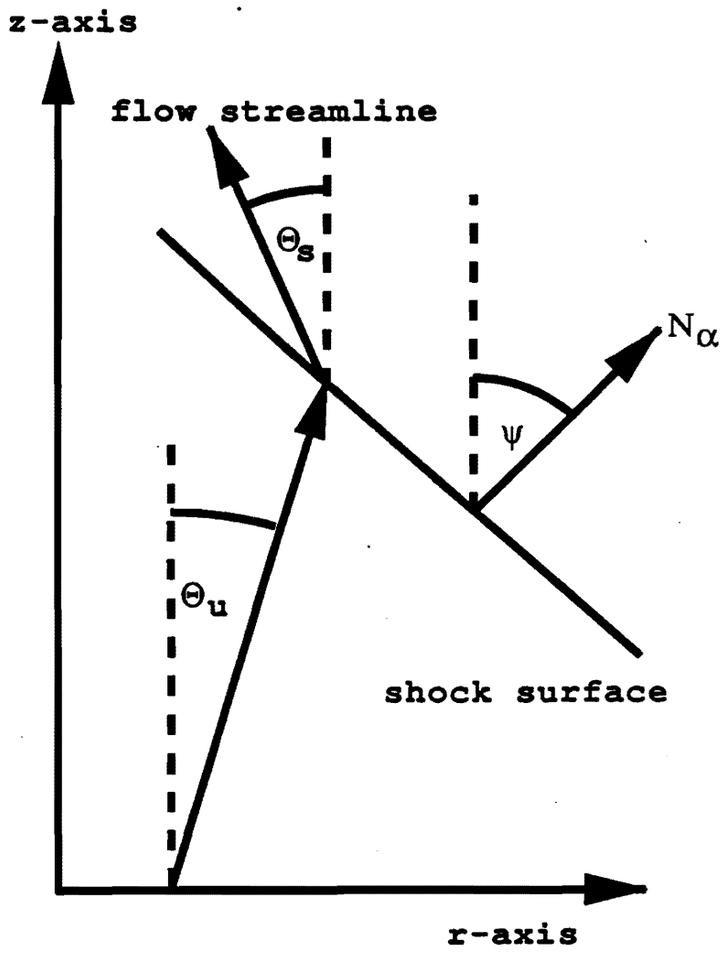
z-axis
flow streamline
Θ_s
N_α
ψ
Θ_u
shock surface
r-axis

Fig 1

(a)

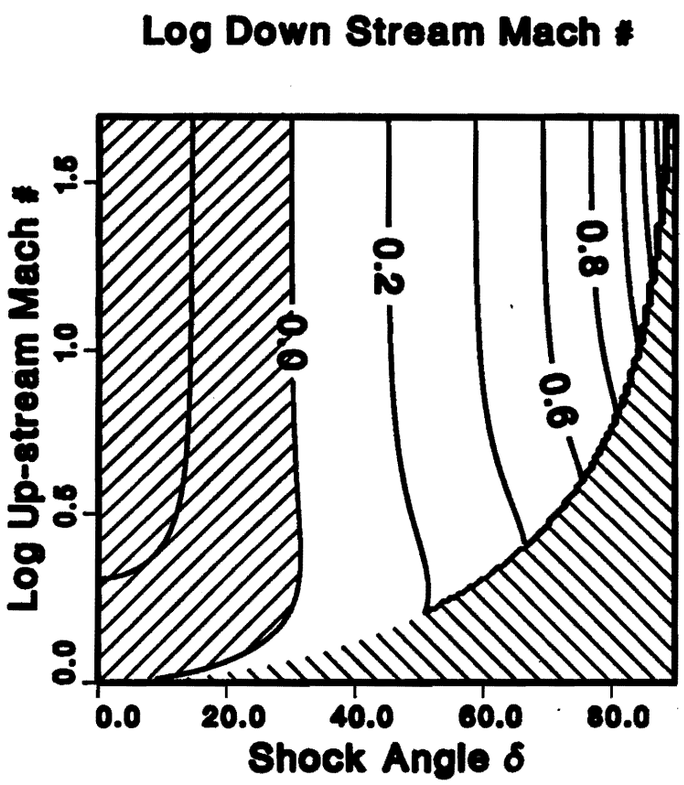
Log Down Stream Mach #
Log Up-stream Mach #
0.0
0.5
1.0
1.5
0.0
0.2
0.4
0.6
0.8
0.0
20.0
40.0
60.0
80.0
Shock Angle δ

(b)

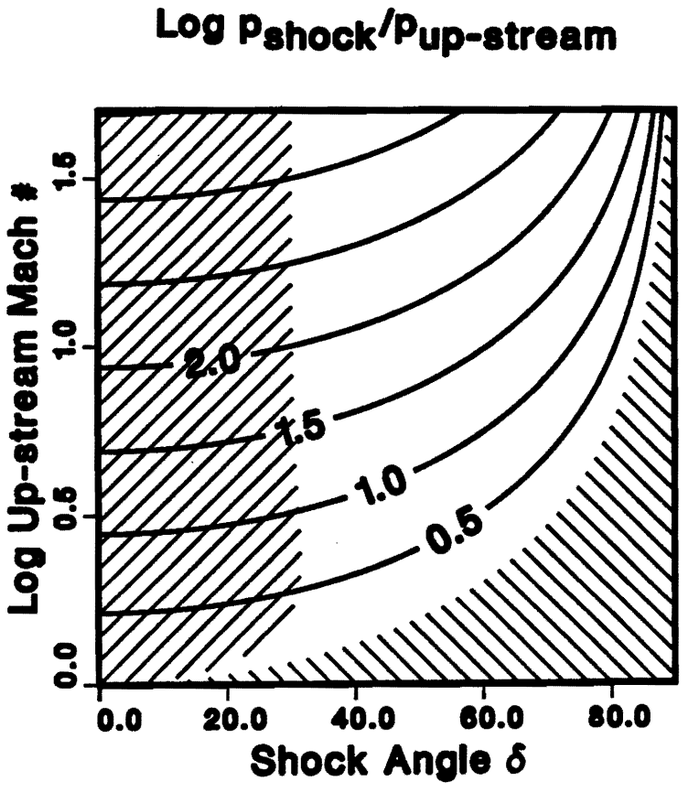
Log $p_{shock}/p_{up\text{-}stream}$
Log Up-stream Mach #
0.0
0.5
1.0
1.5
2.0
1.5
1.0
0.5
0.0
20.0
40.0
60.0
80.0
Shock Angle δ

Fig 2

(a)

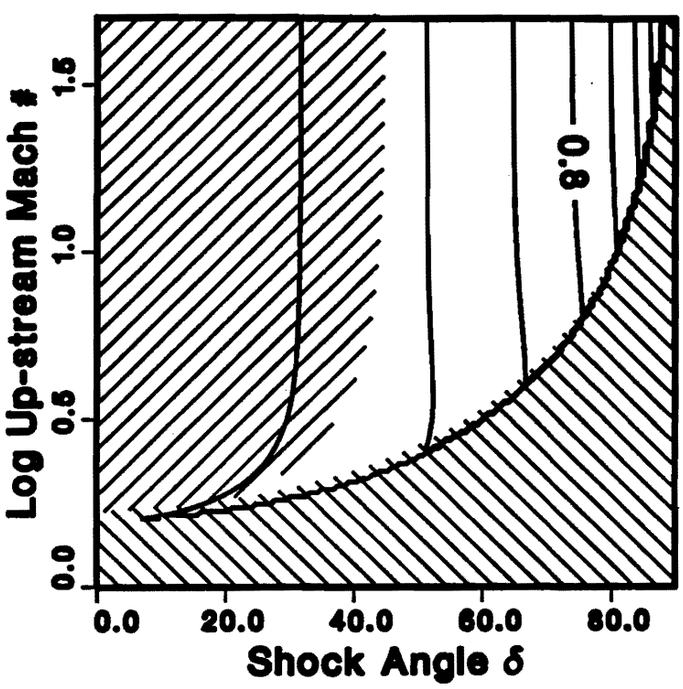
Log Down Stream Mach #
Log Up-stream Mach #
0.0
0.5
1.0
1.5
8.0
0.0
20.0
40.0
60.0
80.0
Shock Angle δ

(b)

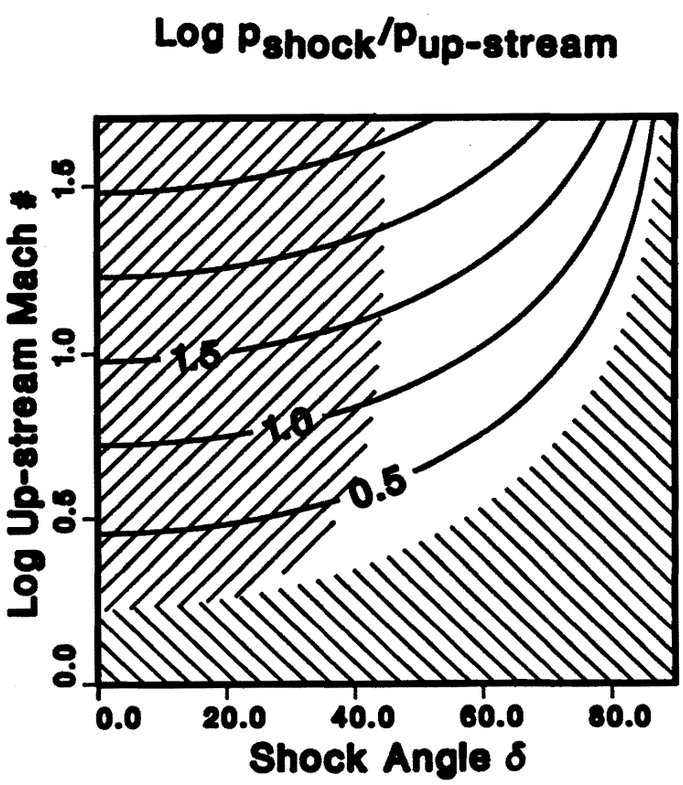
Log $p_{shock}/p_{up\text{-}stream}$
Log Up-stream Mach #
0.0
0.5
1.0
1.5
1.5
1.0
0.5
0.0
20.0
40.0
60.0
80.0
Shock Angle δ

Fig 3

(a)

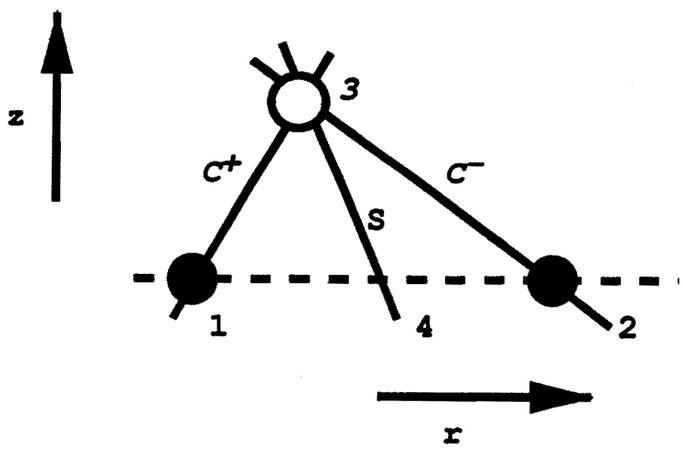

(b)

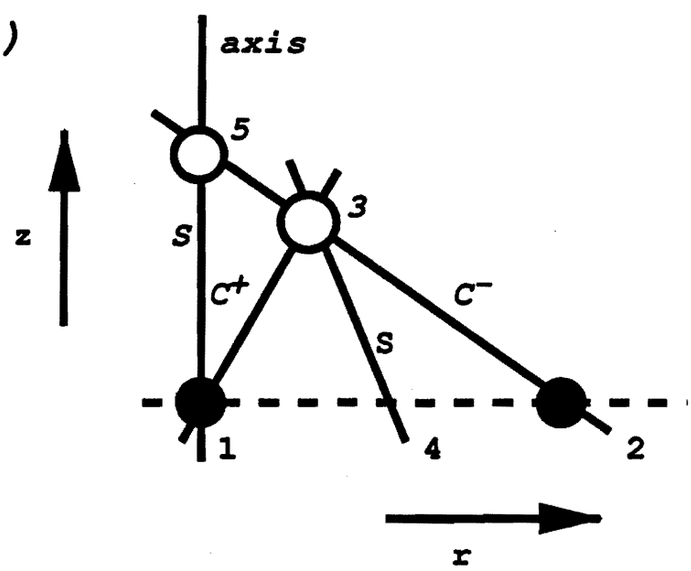

Fig 4

(c)

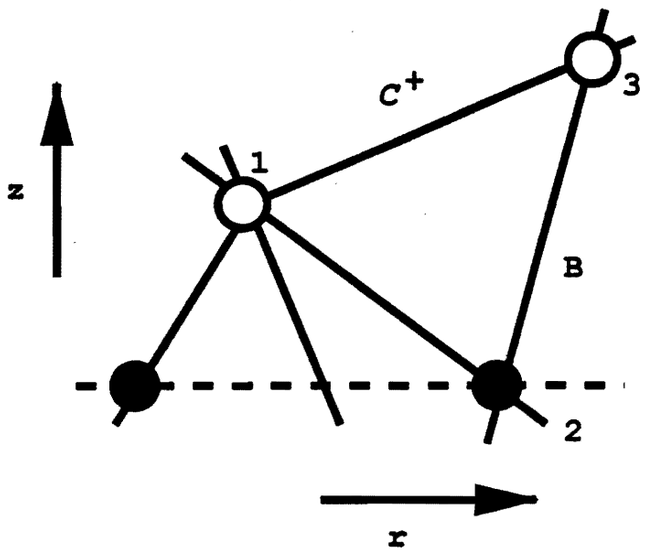

(d)

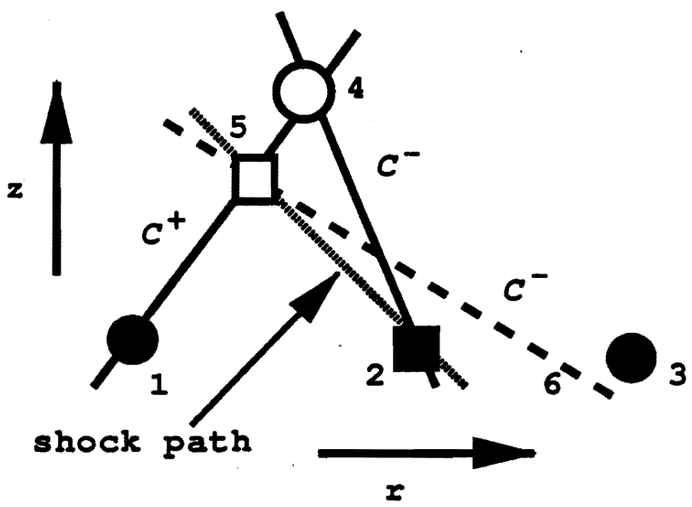

Fig 4 (cont.)

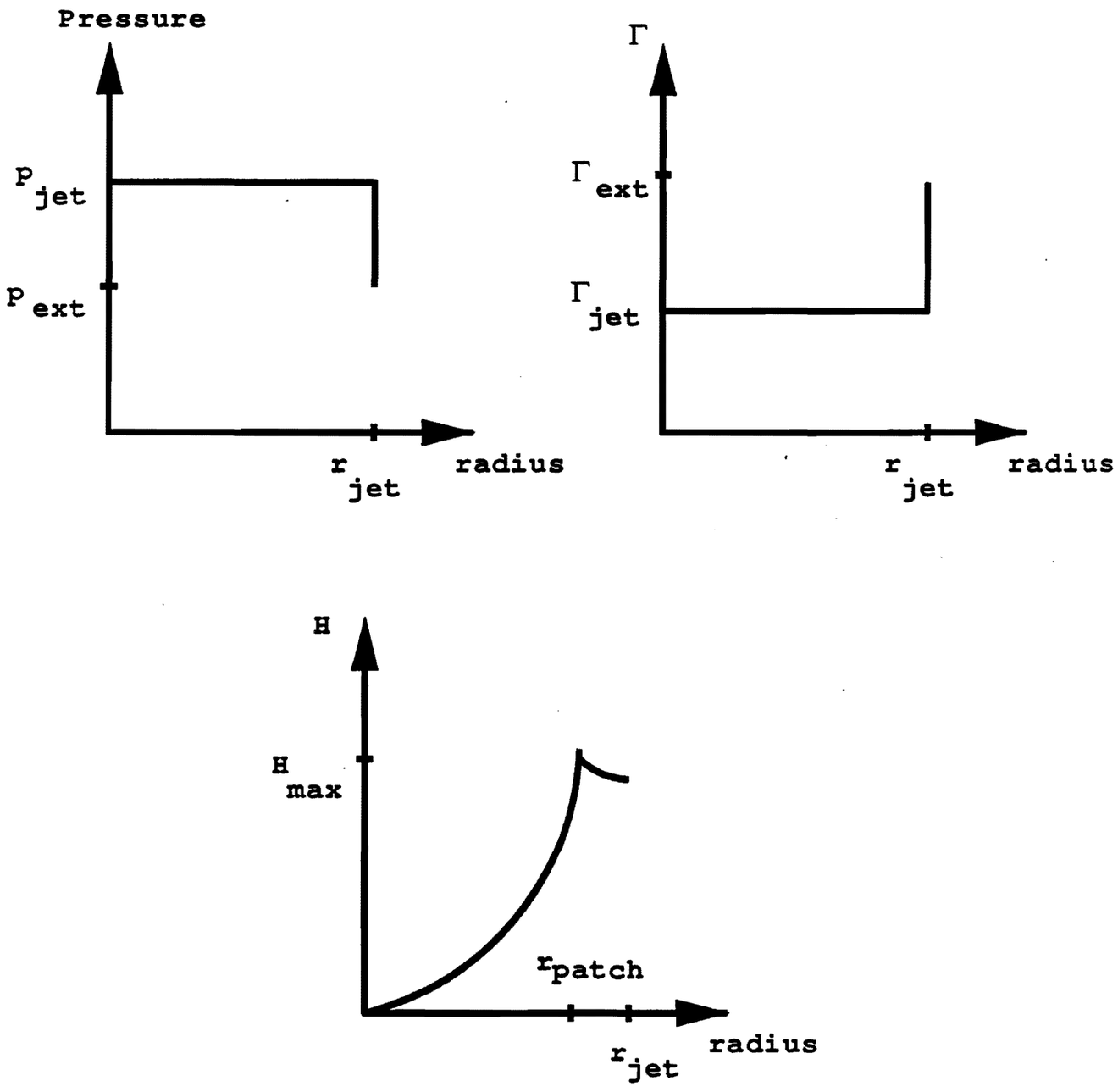
Pressure
p jet
p ext
r jet
radius
Γ
Γ ext
Γ jet
r jet
radius
H
H max
r patch
r jet
radius

Fig 5

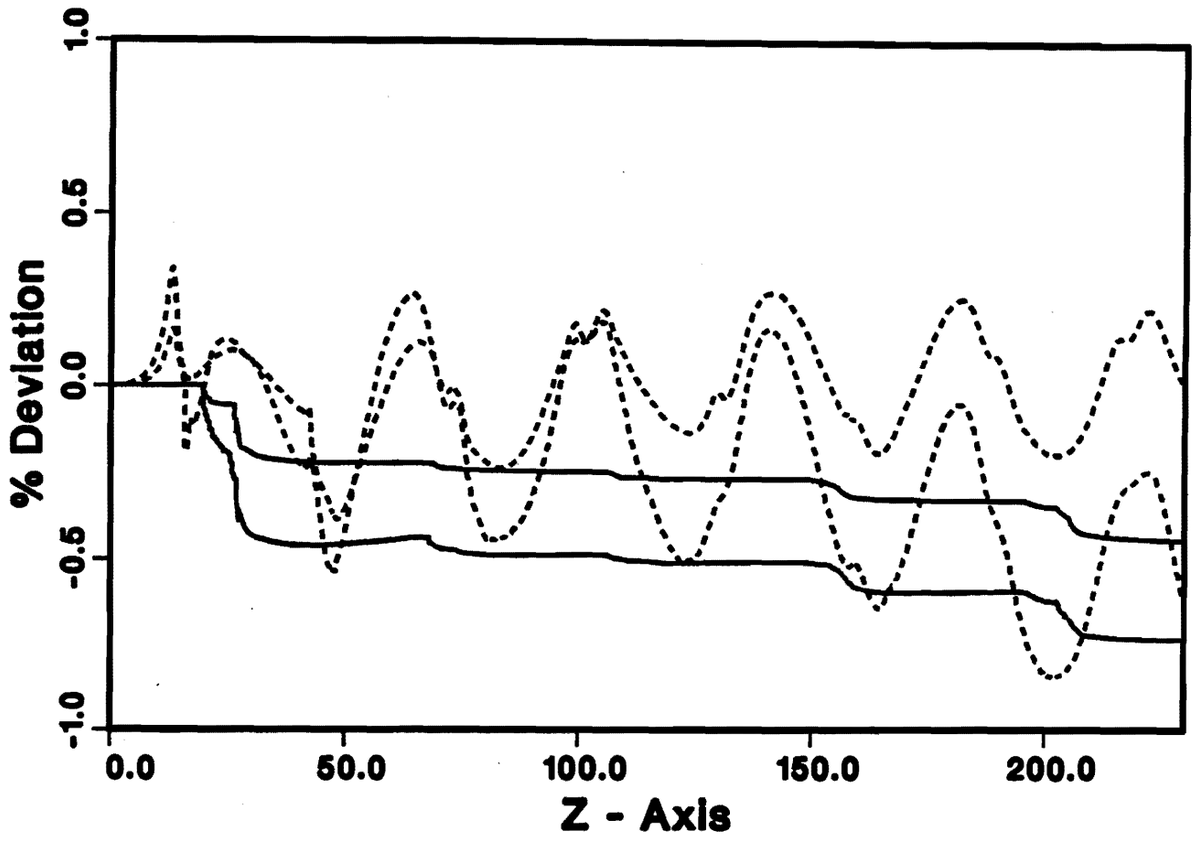

Fig 6

(a)

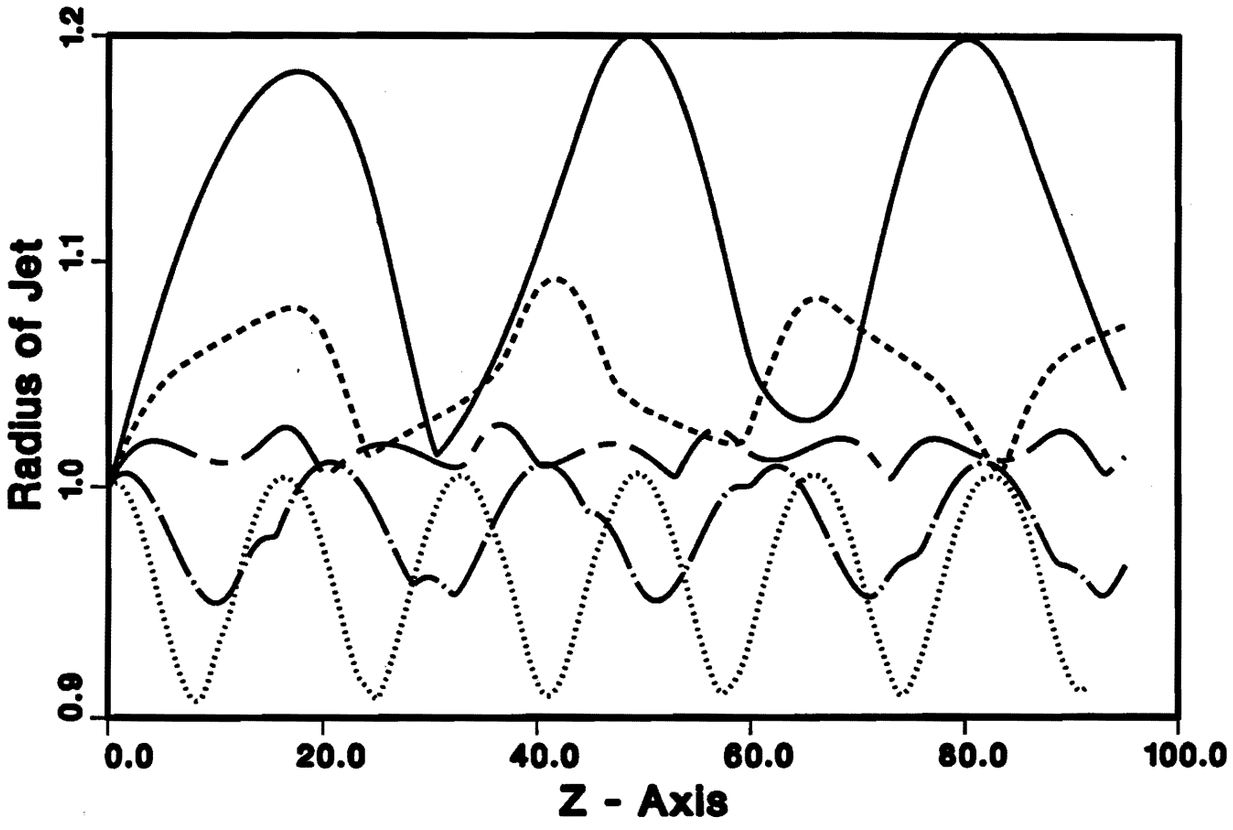
Radius of Jet
1.2
1.1
1.0
0.9
0.0
20.0
40.0
60.0
80.0
100.0
Z - Axis

(b)

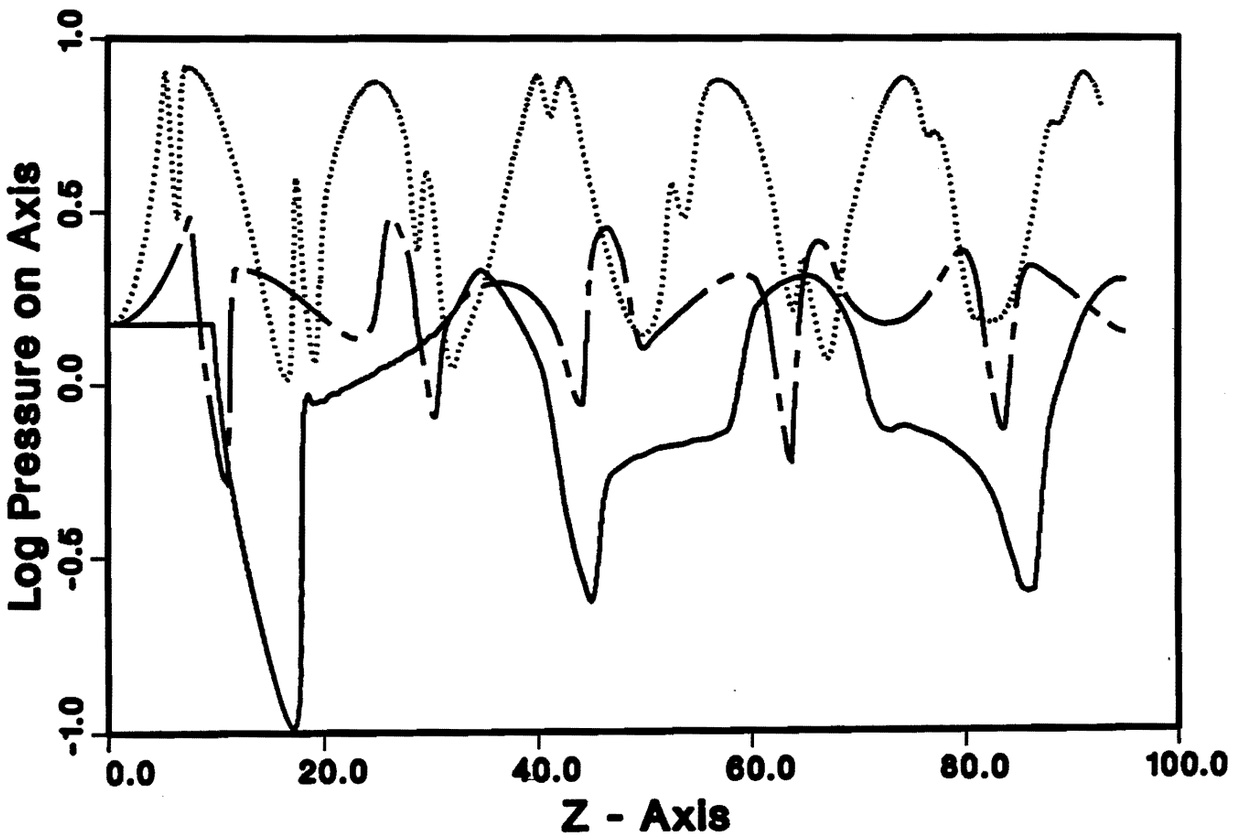
Log Pressure on Axis
1.0
0.5
0.0
-0.5
-1.0
0.0
20.0
40.0
60.0
80.0
100.0
Z - Axis

Fig 7

(c)

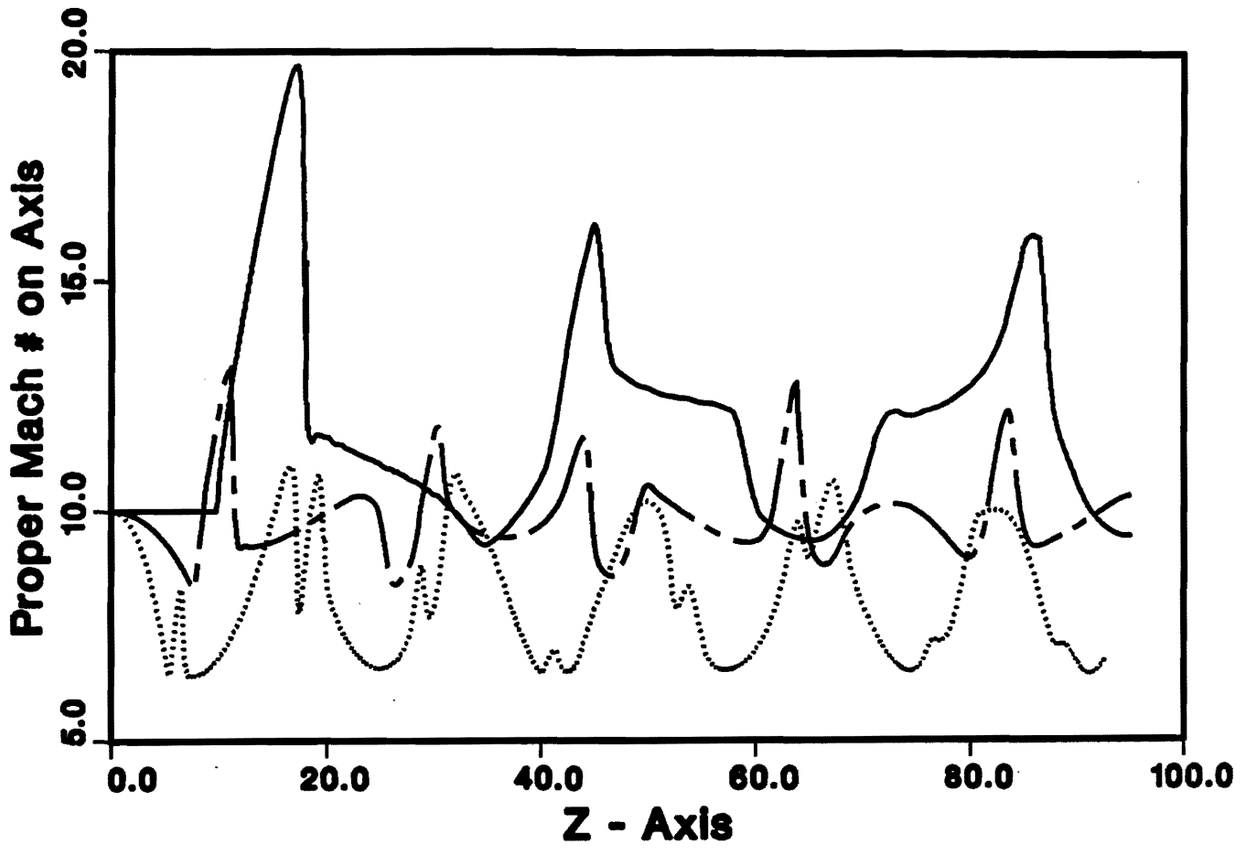

Fig 7 (cont.)

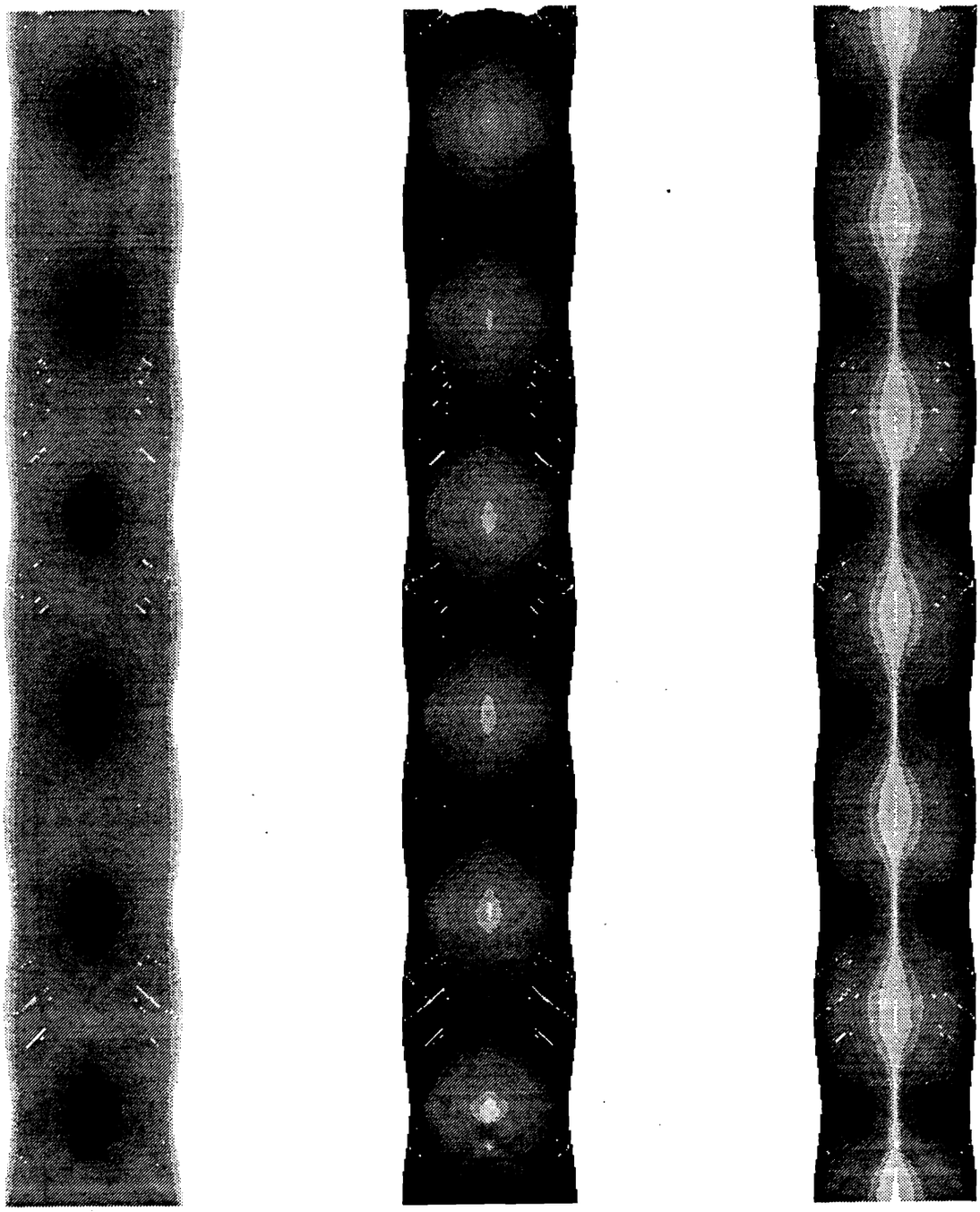

(a) (b) (c)

Fig 8

(a)

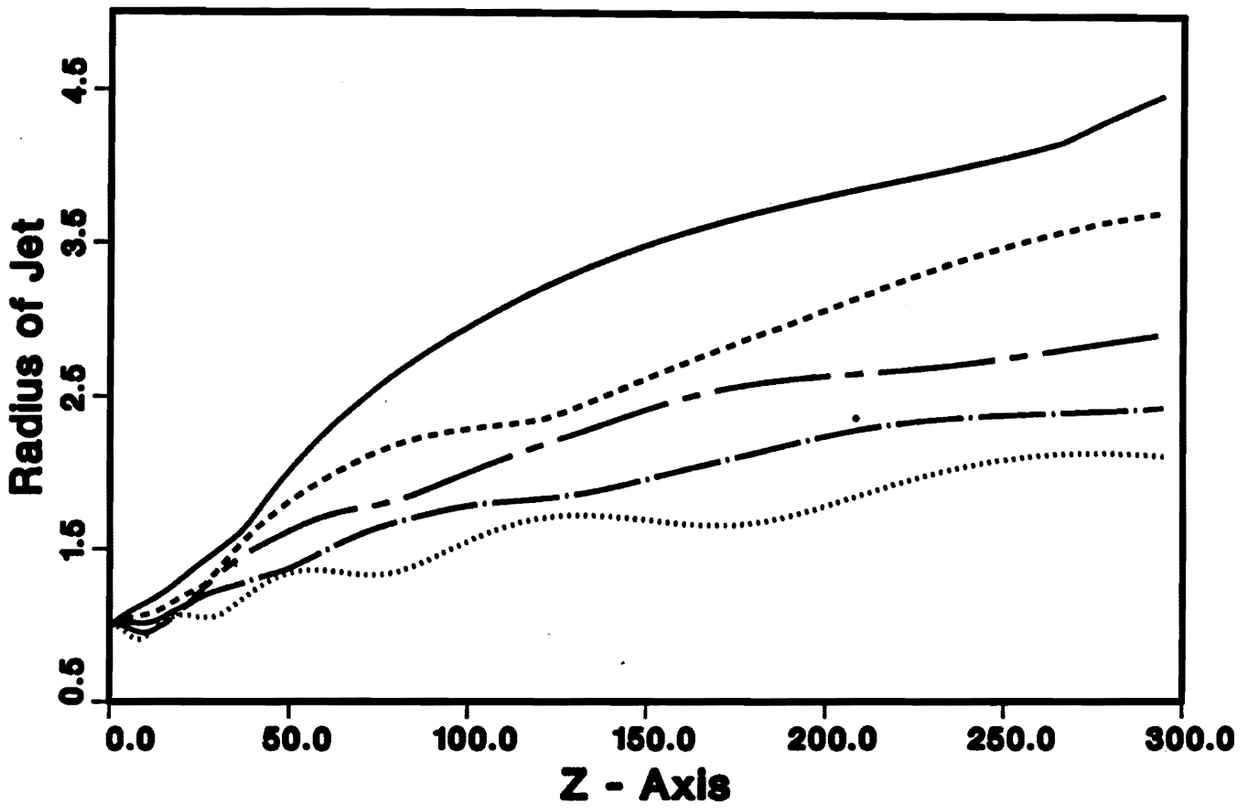
Radius of Jet
0.5
1.5
2.5
3.5
4.5
0.0
50.0
100.0
150.0
200.0
250.0
300.0
Z - Axis

(b)

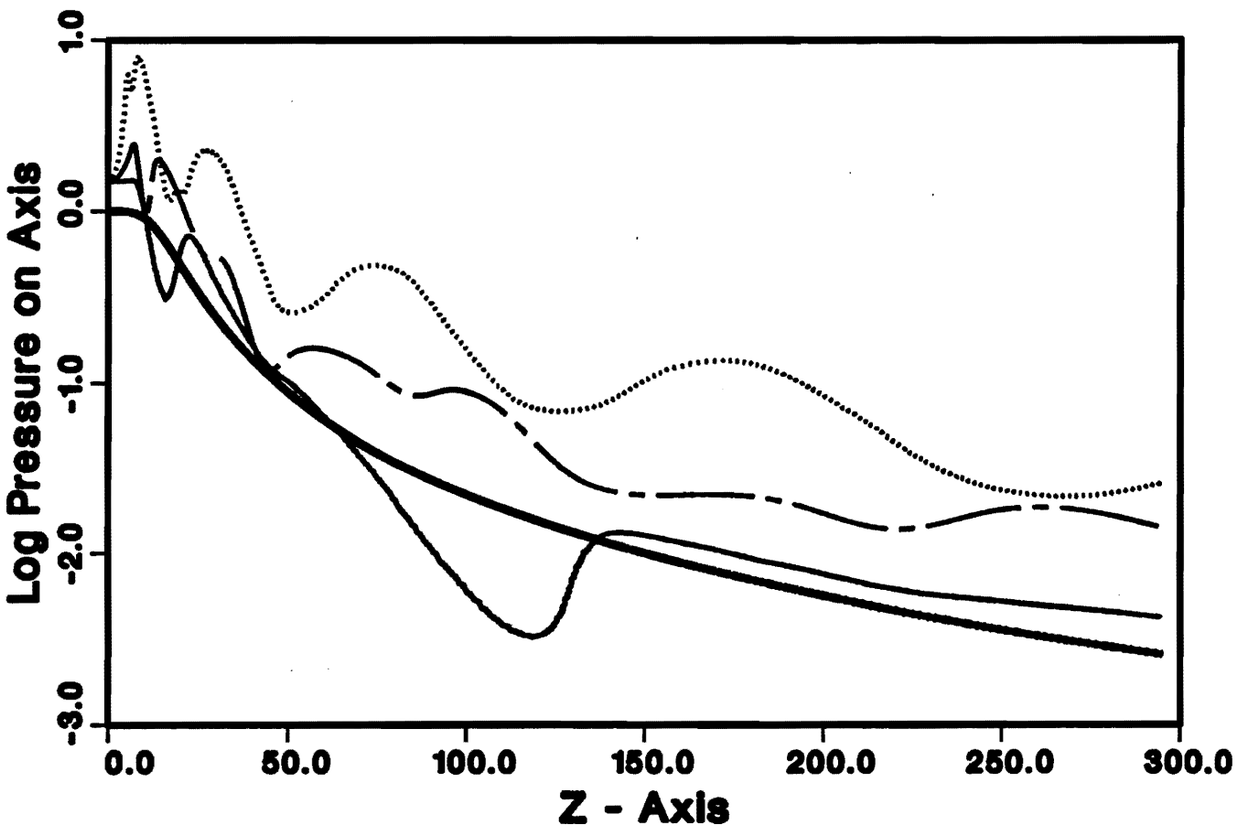
Log Pressure on Axis
1.0
0.0
-1.0
-2.0
-3.0
0.0
50.0
100.0
150.0
200.0
250.0
300.0
Z - Axis

Fig 9

(c)

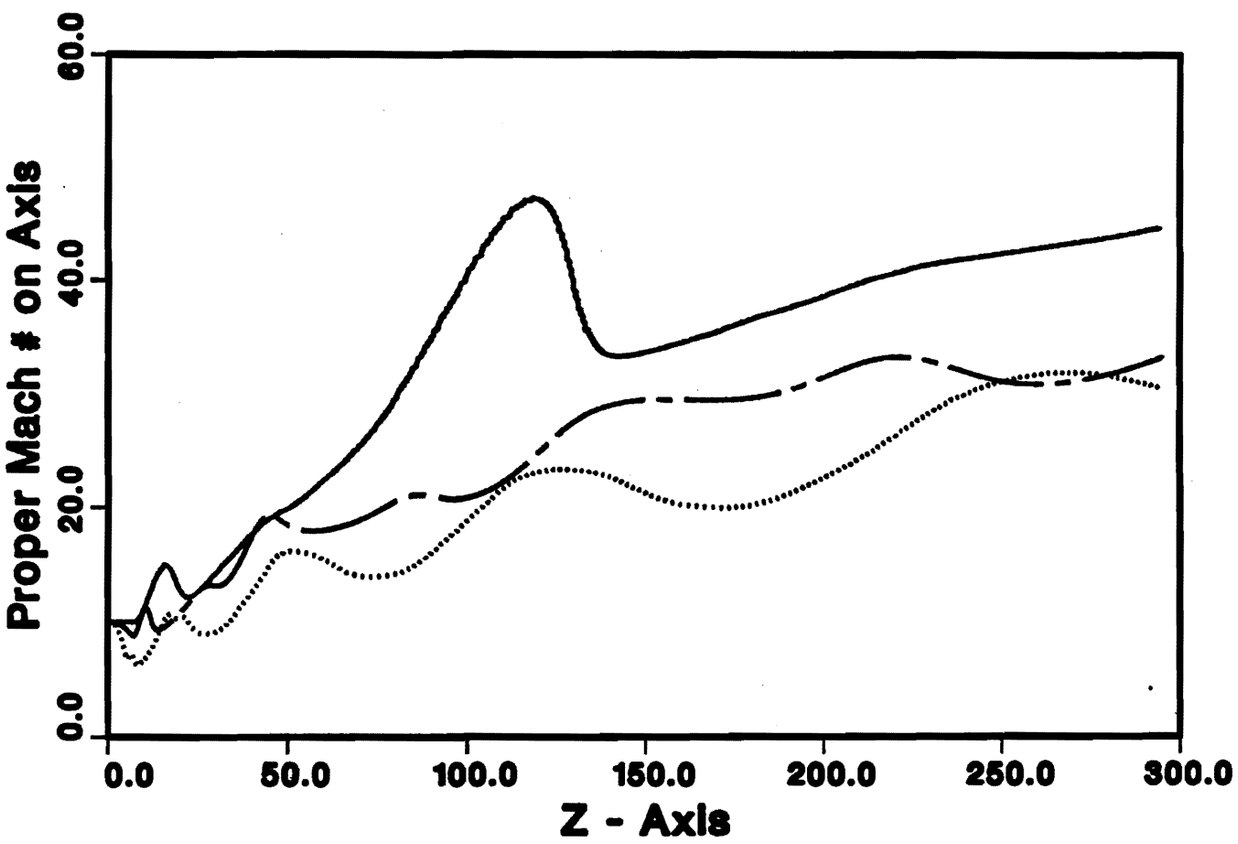

(d)

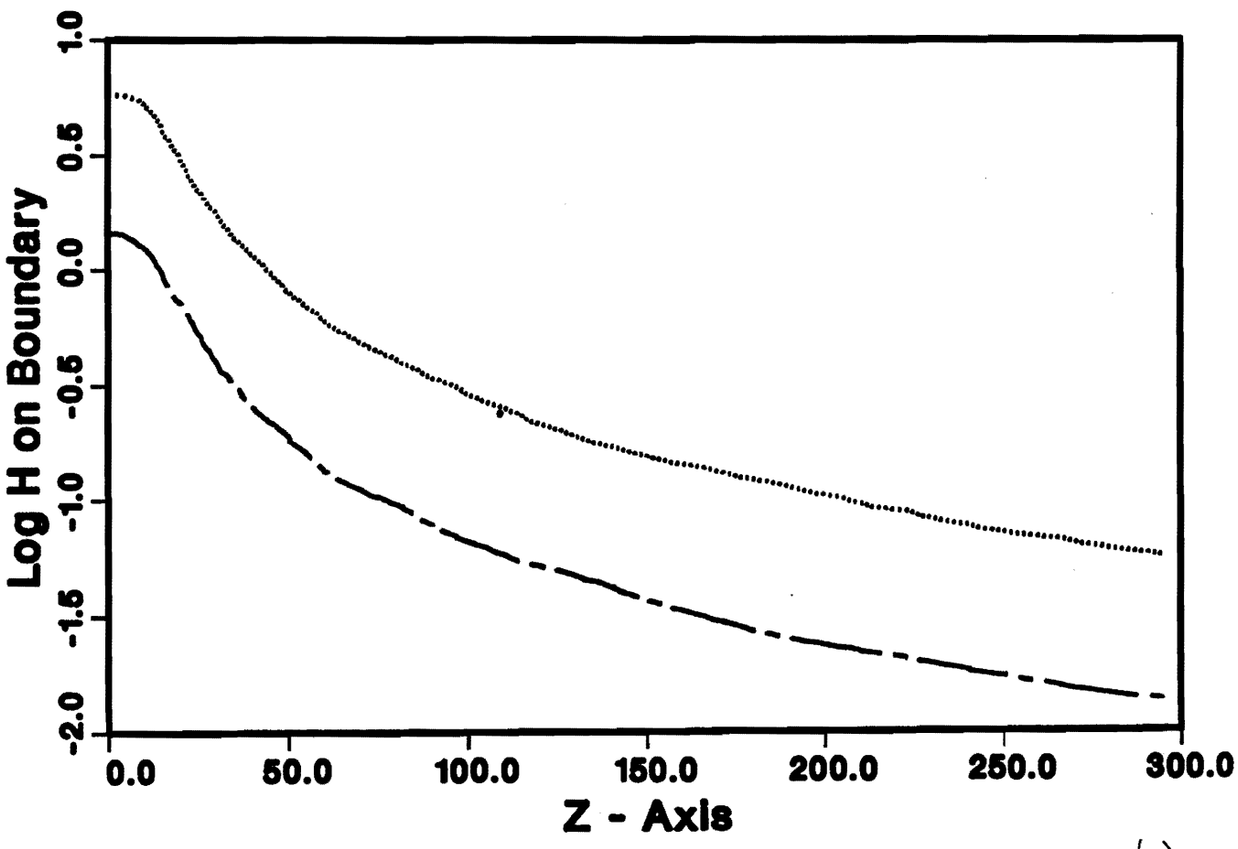

PLOT 1 15.28.25 THUR 7 MAY, 1992 JOB-Mark Dubl University of Texas DISSPLA 11.0

Fig 9 (cont.)

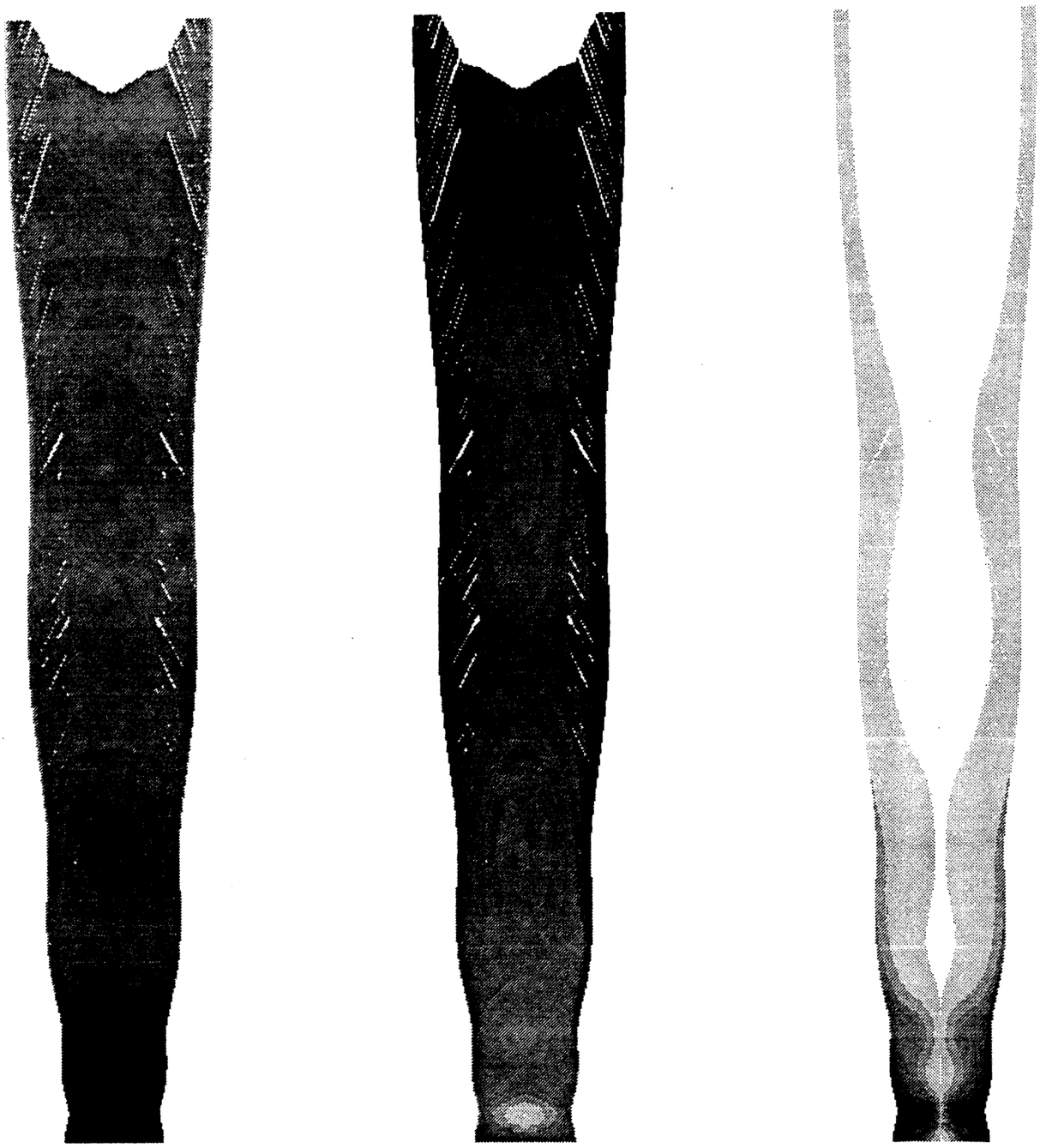

(a) (b) (c)

Fig 10

(a)

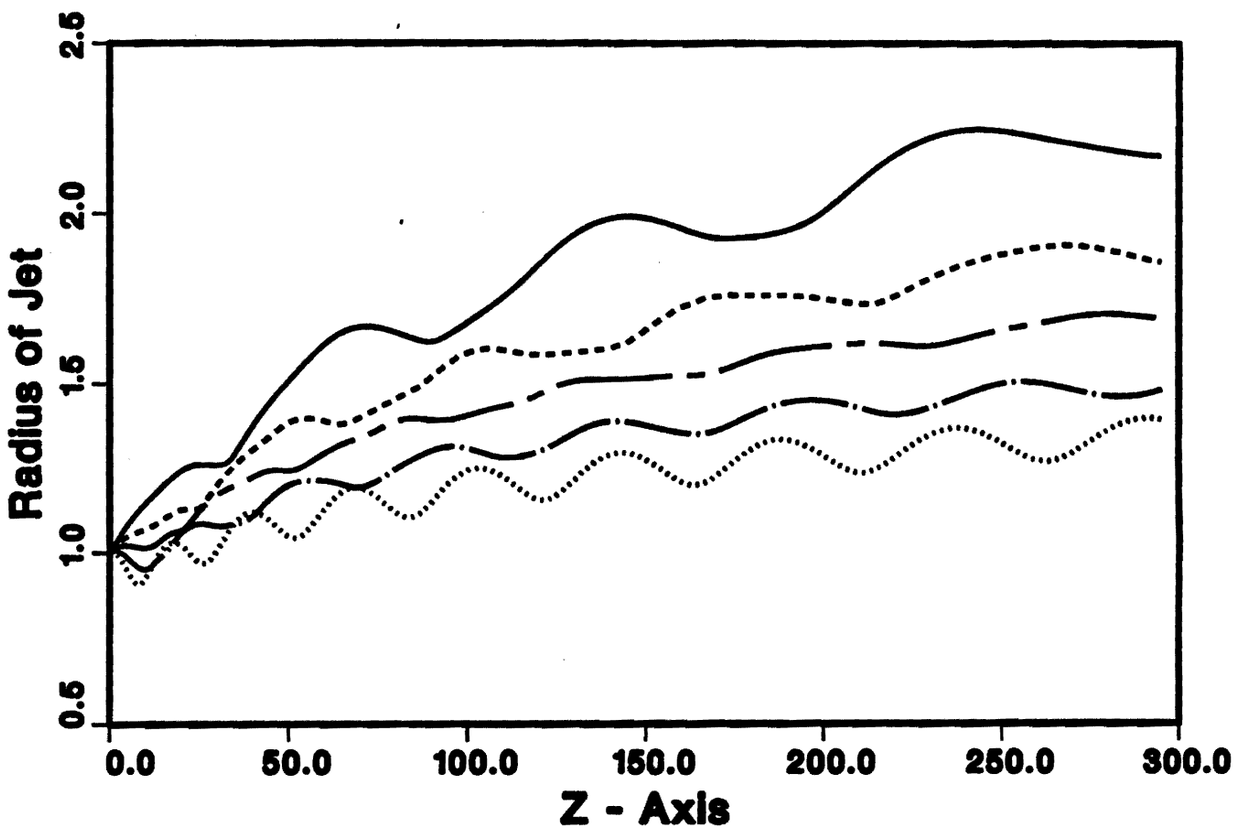
Radius of Jet
2.5
2.0
1.5
1.0
0.5
0.0
50.0
100.0
150.0
200.0
250.0
300.0
Z - Axis

(b)

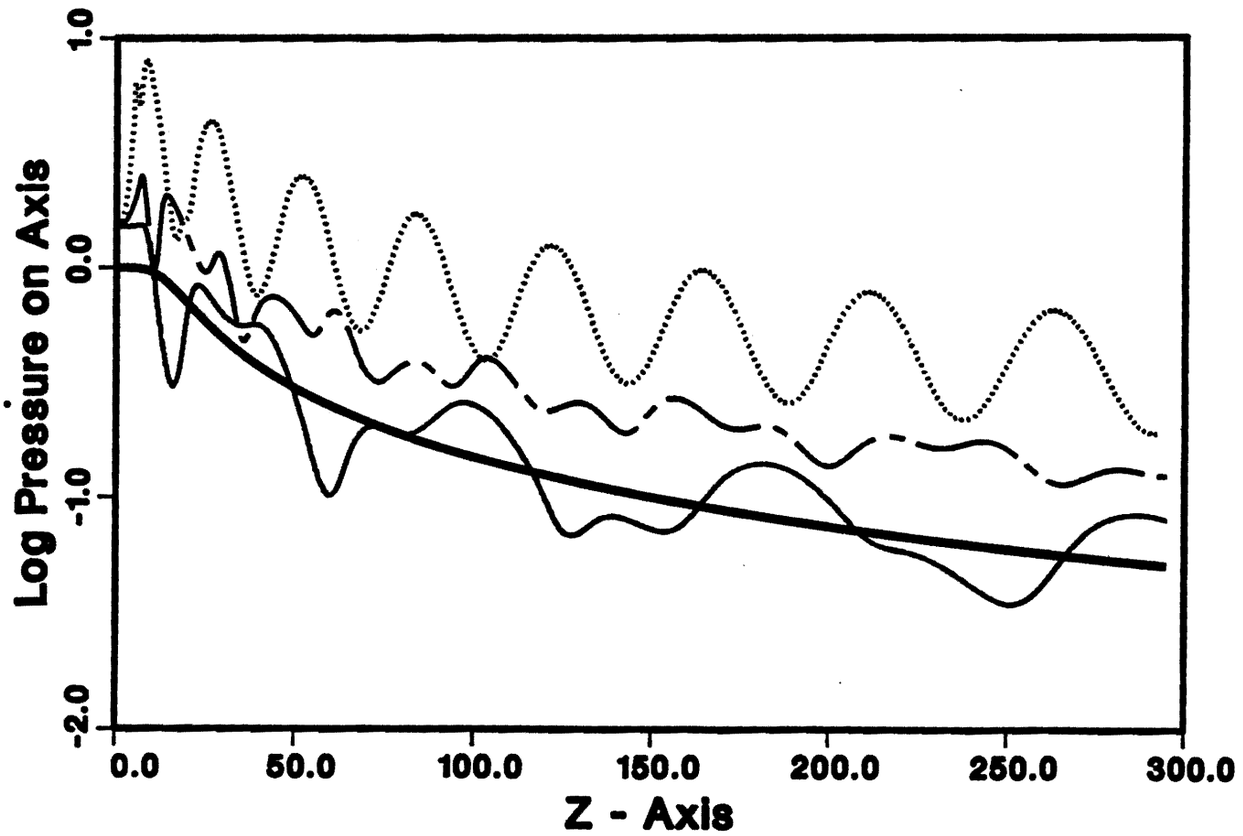
Log Pressure on Axis
1.0
0.0
-1.0
-2.0
0.0
50.0
100.0
150.0
200.0
250.0
300.0
Z - Axis

Fig 11

(c)

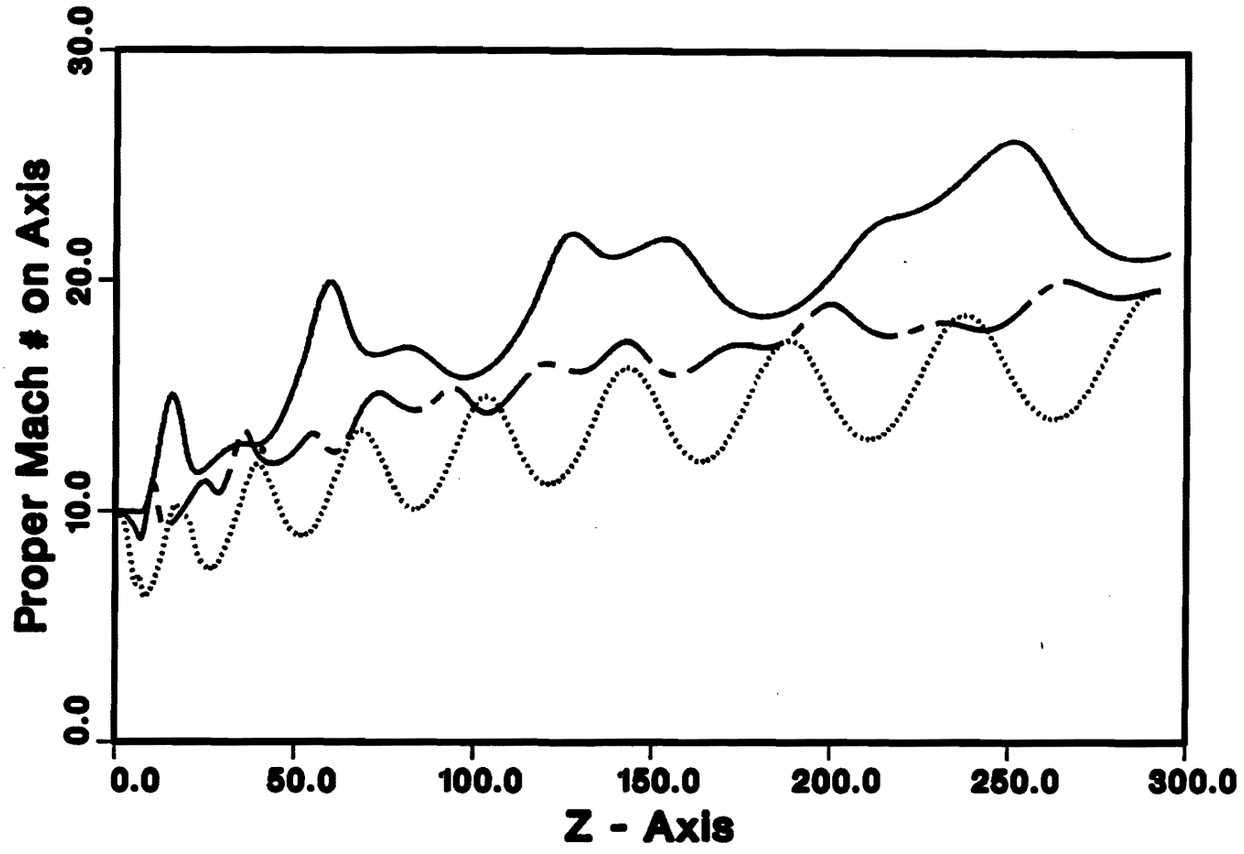

(d)

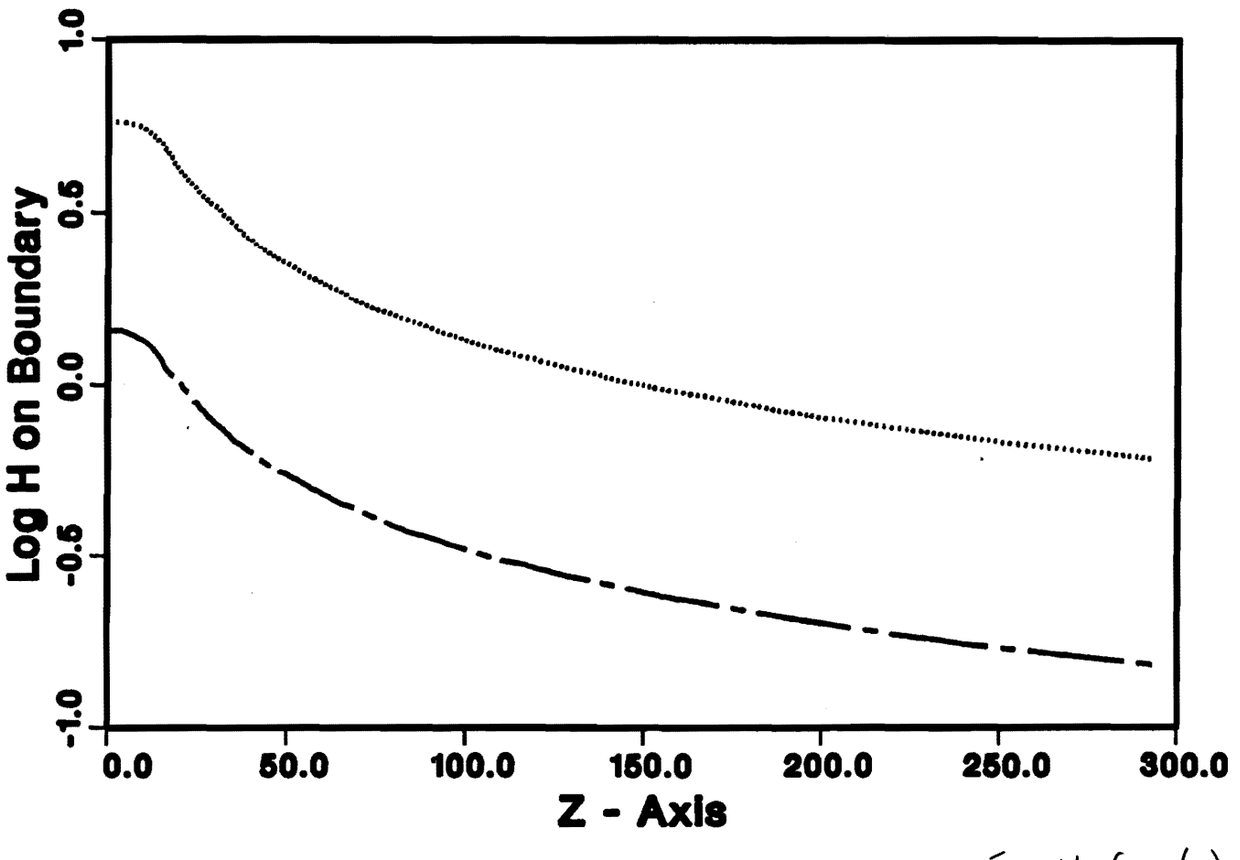

PLOT 1 00.06.37 FRI 6 MAY, 1982 JOB-DUBAL , University of Texas DISSPLA 11.0

Fig 11 (cont.)

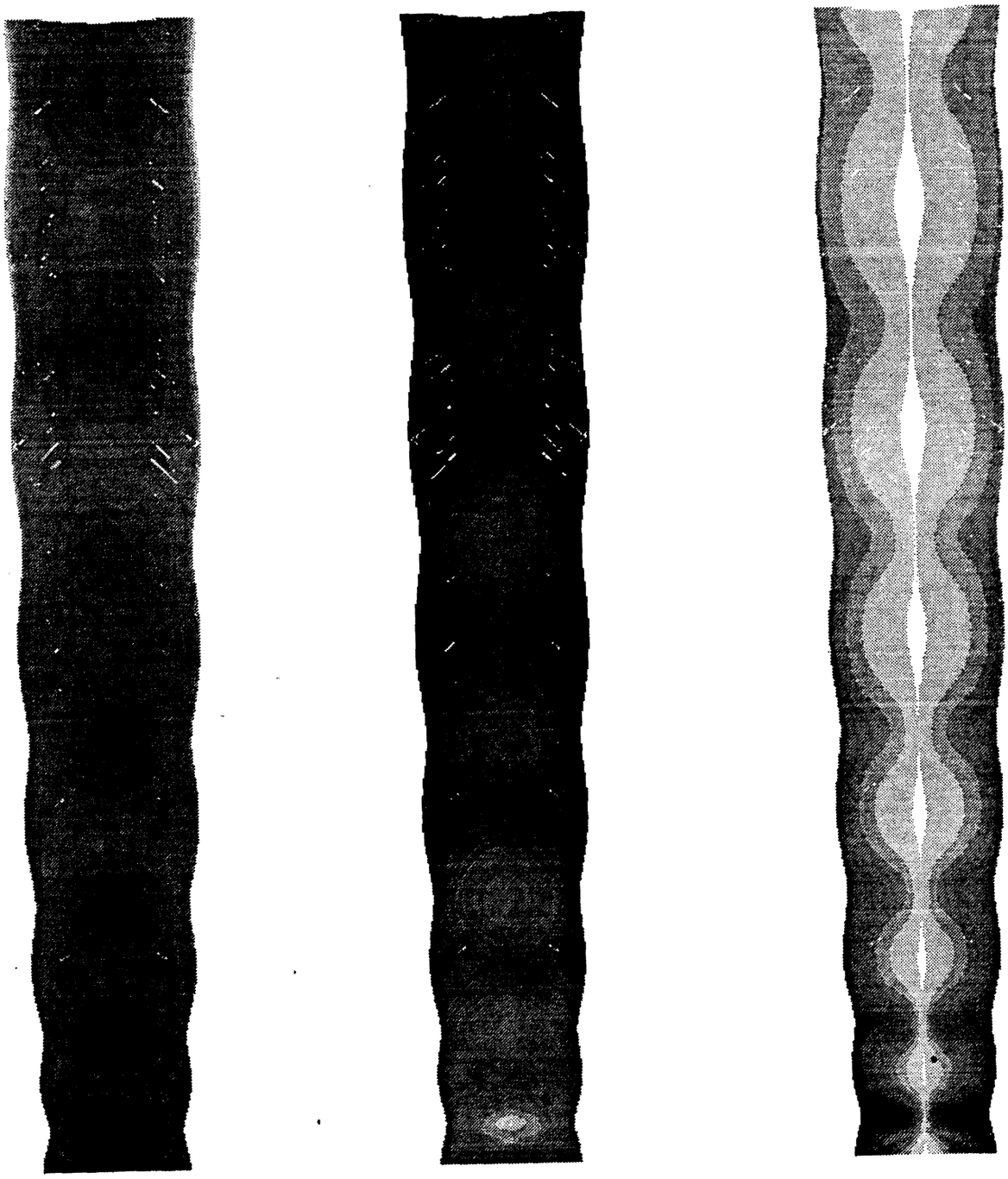

(a) (b) (c)

Fig 12